Reaction Paths of Phosphine Dissociation on Silicon (001)

O. Warschkow[1], N. J. Curson[2,3], S. R. Schofield[2,4], N. A. Marks[1,5], H. F. Wilson[1,6,7], M. W. Radny[8], P. V. Smith[8], T. C. G. Reusch[2], D. R. McKenzie[1], and M. Y. Simmons[2]

[1]*Centre for Quantum Computation and Communication Technology, School of Physics, The University of Sydney, Sydney, NSW 2006, Australia*

[2]*Centre for Quantum Computation and Communication Technology, School of Physics, The University of New South Wales, Sydney, NSW 2052, Australia*

[3]*London Centre for Nanotechnology and Department of Electronic and Electrical Engineering, University College London, 17-19 Gordon Street, London, WC1H 0AH, United Kingdom*

[4]*London Centre for Nanotechnology and Department of Physics and Astronomy, University College, 17-19 Gordon Street, London, WC1H 0AH, United Kingdom*

[5]*Discipline of Physics & Astronomy, Curtin University, GPO Box U1987, Perth, WA, Australia*

[6]*CSIRO Virtual Nanoscience Laboratory, Parkville, VIC 3052, Australia*

[7]*School of Applied Sciences, RMIT University, Melbourne, VIC 3000, Australia*

[8]*School of Mathematical and Physical Sciences, The University of Newcastle, Callaghan, NSW 2308, Australia*

ABSTRACT: Using density functional theory and guided by extensive scanning tunneling microscopy (STM) image data, we formulate a detailed mechanism for the dissociation of phosphine (PH_3) molecules on the Si(001) surface at room temperature. We distinguish between a main sequence of dissociation that involves PH_2+H, PH+2H, and P+3H as observable intermediates, and a secondary sequence that gives rise to PH+H, P+2H, and isolated phosphorus adatoms. The latter sequence arises because PH_2 fragments are surprisingly mobile on Si(001) and can diffuse away from the third hydrogen atom that makes up the PH_3 stoichiometry. Our calculated activation energies describe the competition between diffusion and dissociation pathways, and hence provide a comprehensive model for the numerous adsorbate species observed in STM experiments.

Keywords: Phosphine; Si(001) surface; Dissociation mechanism; Surface reactions; Surface diffusion; Density functional theory.

I. INTRODUCTION

Phosphine (PH_3) is a common source of phosphorus in the chemical vapor deposition of n-type silicon for the semiconductor industry [1]. The dissociation chemistry of PH_3 on the silicon (001) surface is therefore of considerable technological relevance and has been the subject of numerous experimental [2-20] and theoretical studies [16-18,21-29]. Over the last decade, interest in this reaction system has dramatically increased due to its relevance to ongoing efforts [30-41] to fabricate Si:P quantum electronic devices that operate at the level of single atoms, electrons, and spins. A critical challenge in the fabrication of such devices is the requirement that single phosphorus dopant atoms are placed into crystalline silicon with high spatial precision. An important milestone towards this aim, namely the nanometer-precise placement of single phosphorus atoms on the silicon (001) surface has been demonstrated experimentally [40-43] using the method of scanning tunneling microscopy (STM) hydrogen lithography [44-47]. This has recently culminated in the fabrication of a single-phosphorus-atom transistor [40]. Further developments of this technology towards increased reliability, precision, and scalability are highly desirable. A thorough understanding of the underlying elementary processes of PH_3 adsorption and dissociation on the Si(001) surface is central to this effort.

In previous communications on the PH_3/Si(001) reaction system, we have characterized the three most common dissociation intermediates as PH_2+H, PH+2H and P+3H [16, 17] and have reported observations in which PH_2 fragments migrate over the surface [18]. We have also provided a reinterpretation of previously misunderstood spectroscopic measurements [27] and have investigated phosphorus atom diffusion, incorporation, and thermal desorption pathways on the surface [28, 29]. Collectively, these works were underpinned by detailed scanning tunneling microscopy (STM) experiments in which several intermediates of the PH_3/Si(001) reaction system became apparent as distinct features in the images. A typical room-temperature STM image illustrating some of the phosphine-related surface features on silicon is shown in Fig. 1.

Here we tie together these prior results using new STM image data and a high-quality density functional theory approach in which the effects of finite cluster size and basis set size are tightly controlled. We describe the various competing reaction pathways taken by a phosphorus atom during its transition from a component of a PH_3 gas phase molecule to a dopant adatom on the surface. For the previously described main sequence of phosphine dissociation species (PH_2+H, PH+2H, and P+3H) our DFT calculations fill the temporal gap between the long-lived species observable on STM imaging timescales (minutes per frame) and other intermediates that are too short-lived to be imaged. One of these short-lived species

is the PH_2 fragment and we will describe how the rapid diffusion of PH_2 gives rise to an alternative reaction sequence that produces several additional species (PH+H, P+2H, and isolated phosphorus adatom). Also produced as a result of PH_2 diffusion are isolated hemihydride dimers of which two can be seen in Fig. 1. The reaction sequences we present highlight the subtle balance of reaction pathways that ultimately determine the final state of the surface.

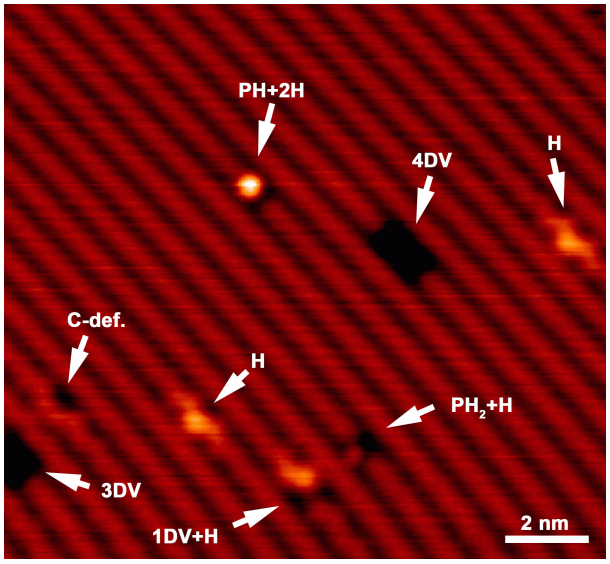

FIG. 1: (a) Large-scale filled-state STM image of a silicon (001) sample exposed to a low dosage of phosphine gas. Several kinds of surface features are apparent: hemihydride dimers (H), C-defects (i.e. dissociated water), three- and four-dimer vacancies (3DV and 4DV, respectively), and a hemihydride adjacent to a dimer vacancy (1DV+H). Two features related to PH_3 exposure are the asymmetric feature (PH_2+H) and the centered feature (PH+2H), which are characterized, respectively, by a row-offset and row-centered protrusion. The image was recorded using a sample bias of -2.0 V.

II. METHODOLOGY

A. Computational Methodology

All calculations reported in this work are based on density functional theory (DFT) and methods of geometry optimization, transition-state search, and normal-mode analysis as implemented in the *Gaussian 09* software [48]. Adsorption energies are calculated using a *cluster composite model (CCM;* Refs. 49 and 50) that has a proven track record of describing surface chemisorption processes on elemental semiconductor surfaces in conjunction with STM experiments [50-56]. The CCM combines the results of several low-level contributor calculations to provide an economic estimate of energies that would be obtained by a single high-level calculation. High and low level refer here to a triad of near-independent approximations that must be adequately managed, namely, the exchange-correlation treatment, the size of the cluster representation of the surface, and the quality of the Gaussian-type basis set. Ideally, one would want to combine a high-

quality hybrid-DFT treatment with a cluster large enough to minimize boundary effects and a basis set flexible enough to minimize superposition effects. However, an *all-in-one* calculation with all three approximations treated at a high level is impractically expensive. The CCM overcomes this problem by pairing every high-level approximation with a more economic low-level approximation to estimate "all-high-level" adsorption energies as a sum of mixed high- and low-level calculations. Specifically, adsorption energies in the CCM approach, ΔE^{CCM}, are calculated using the expression

$$\Delta E^{CCM} = \Delta E(H/H//H/L, L) + [\ \Delta E(L/L,H) - \Delta E(L/L,L)\ ] + \Delta ZPC(H/L, L) \qquad (1)$$

where the terms ΔE(*functional/basis set*, *cluster model*) refer to separate energy calculations in which the DFT functional, basis set, and cluster model are a combination of high (H) and low levels (L) as indicated. In line with standard quantum chemistry notation we use a single forward slash character ('/') to describe the combination of DFT functional and basis set used. A double forward slash ('//') indicates that different functional/basis set combinations were used for single point energy calculations and geometry optimizations (left and right hand side of '//', respectively). We further use a 'Δ' character to indicate that these energies are given relative to a separated bare surface cluster and a gas-phase molecule; i.e. all the individual ΔE terms in Eq. 1 are calculated as a difference of total energies, E, as follows

$$\Delta E = E_{cluster+molecule} - E_{cluster} - E_{molecule}. \qquad (2)$$

With these notational devices, the first term on the right-hand-side of Eq. 1 describes an H/H high-level functional and basis set calculation of the adsorption energy for a low-level (i.e. small) cluster model. The cluster is geometry optimized using an H/L pairing of a high-level functional and low-level basis set. The second and third term enclosed in square brackets provide a cluster-size-correction, in which an L/L combination of low-level basis set and functional is used in two calculations to estimate the effects of increasing the cluster size from low-level to high-level (i.e. from a small to a large cluster). The fourth term represents a vibrational zero point correction, which is calculated via a harmonic vibrational frequency calculation using the high-level DFT functional, a low-level basis set, and a low level cluster.

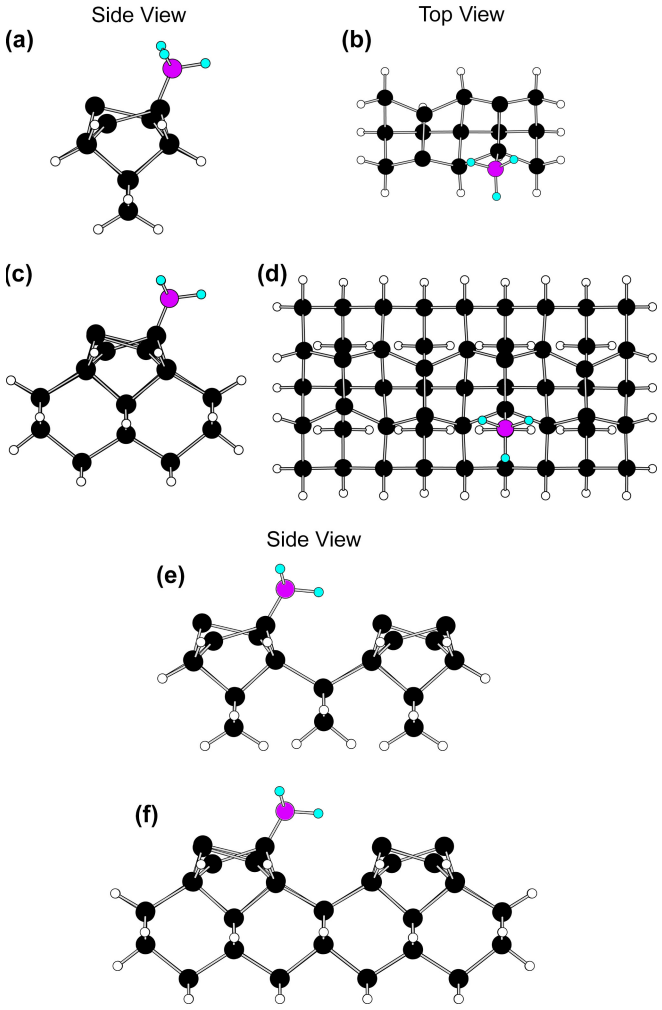

Figure 2: Side- and top-view illustration of cluster models used in this work. (a,b) A small, two-dimer $Si_{15}H_{16}$ cluster, denoted 2D1R4L in the text, and (c,d) a larger four-dimer $Si_{53}H_{44}$ cluster denoted 4D1R5L. Together these two clusters are used as the low- and high-level size approximation of the 2D1R cluster composite model. (e) A double-row $Si_{49}H_{40}$ cluster with three dimers per row, denoted 3D2R4L. (f) A double-row $Si_{119}H_{80}$ cluster with five dimers per row, denoted 5D2R5L. These two double-row clusters are used as the low- and high-level size approximation in the 3D2R composite model. The specific adsorption structure shown is molecularly adsorbed PH_3, which is referred to as structure A1 in the text.

The specific settings used here for high- and low-levels of theory are summarized in Table I. For the exchange-correlation treatment we pair a hybrid-DFT functional (B3LYP; Refs. 57 and 58) with the generalized gradient approximation (GGA; PW91 functional; Refs. 59 and 60) as high and low levels, respectively. We note that neither of these two functionals includes any empirical, atom-pairwise correction terms to account for dispersion effects. Dispersion is unlikely to significantly influence the adsorption reactions of a small adsorbate molecule (PH_3) that forms strong covalent bonds with the silicon surface. In order to define the basis set, it is convenient to group the atoms of the cluster and molecule atoms into three subsets according to their relevance to the adsorption process: subset A refers to all atoms of the adsorbate and all surface Si-Si dimers, subset B refers to all atoms of the second (i.e. subsurface) atomic layer, and subset C refers to all other

cluster atoms including the cluster-terminating hydrogen atoms. As a high-level basis set, we use a standard 6-311G(2df,2pd) Gaussian-type atomic set for all three subsets of atoms and we further augment this basis set with additional "++" diffuse functions for the atoms of subset A; i.e. those atoms immediately involved in the adsorbate-surface interaction. The corresponding low-level basis set is more compact, using fewer polarization functions for subsets A and B [namely, (d,p) polarization instead of (2df,2pd)] and a LANL2DZ double-zeta pseudopotential basis set for subset C. We note in passing that the low-level basis set is in our experience entirely sufficient for conducting structure optimizations [see e.g. Table 4 in Ref. 49]. The purpose of the larger basis set is to improve the accuracy of the calculated energy at the optimized geometry as indicated by the notation H/H//H/L in the first term of Eq. 1.

The size of the clusters used to represent the surface is determined by the chemistry in that *at least* all the Si-Si surface dimers involved in a chemical reaction must be included in the cluster model in both the high and low level components of the CCM. In this work, a large fraction of the reactions play out on two adjacent dimers. Accordingly, we use a two-dimer $Si_{15}H_{16}$ cluster [Fig. 2(a,b)] as a low-level representation of the surface. We denote this cluster as 2D1R4L in short to indicate its size in dimers (D), dimer-rows (R), and atomic layers (L). The corresponding high-level, large cluster is extended by one dimer along both row directions and increased in depth by one atomic layer. This produces a four-dimer $Si_{53}H_{44}$ cluster that is labeled 4D1R5L and is shown in Fig. 2(c,d). This particular pairing of 2D1R4L and 4D1R5L low- and high-level clusters is used in the majority of calculations in this work. Collectively, we refer to this cluster pairing as the 2D1R cluster composite model, indicating the numbers of dimers and rows that are represented in the low-level cluster and are therefore subject to a high-level exchange-correlation and basis set treatment (see first term of Eq. 1).

A few of the reaction steps we consider require more than two adjacent dimers or more than a single dimer row. In order to describe these processes we define two additional cluster pairings in Table I. The pairing of 3D1R4L and 5D1R5L clusters ($Si_{21}H_{20}$ and $Si_{65}H_{52}$, respectively) defines the 3D1R cluster composite model, which is an extension of the 2D1R model by one Si-Si dimer along the row. This model allows us to describe adsorbate configurations and reactions that extend over three dimers. The pairing of 3D2R4L and 5D2R5L clusters [$Si_{49}H_{40}$ and $Si_{119}H_{80}$, respectively, and Figs. 2(e) and (f)] defines the 3D2R composite model, which corresponds to a widening of the 3D1R model by a second row. In this pairing, the low-level cluster represents six surface dimers on two adjacent rows (i.e. three dimers per row), while the high-level cluster is again an extension by one dimer along each row for a total of ten dimers. We will use the 3D2R composite model to describe

reactions in which molecular fragments shift from one dimer row to the next. Such inter-row reactions are surprisingly important to the PH_3/Si(001) chemistry as we will describe below.

	Low Level (L)	**High Level (H)**
Exchange-Correlation	GGA (PW91)	Hybrid-DFT (B3LYP)
Basis Set	(A) 6-311++G(d,p) (B) 6-311G(d,p) (C) LANL2DZ	(A) 6-311++G(2df,2pd) (B) 6-311G(2df,2pd) (C) 6-311G(2df,2pd)
Cluster Model – 2D1R	2D1R4L ($Si_{15}H_{16}$)	4D1R5L ($Si_{53}H_{44}$)
Cluster Model – 3D1R	3D1R4L ($Si_{21}H_{20}$)	5D1R5L ($Si_{65}H_{52}$)
Cluster Model – 3D2R	3D2R4L ($Si_{49}H_{40}$)	5D2R5L ($Si_{119}H_{80}$)

Table 1: Overview of the pairings of low- and high-level approximations in our cluster composite model (CCM) approach in regards to exchange-correlation, Gaussian-type basis set, and type of cluster representation of the surface. The low- and high-level basis sets are composed of standard Gaussian atomic sets, with three different sets applied to three types of atoms (A), (B), and (C), as defined in the text. Also listed are three types of cluster model pairings that are labelled 2D1R, 3D1R, and 3D2R, indicating the number of surface dimers (D) and rows (R) represented in the low-level sized cluster. The corresponding high-level sized clusters are extended by one dimer in each direction along the dimer row, and one additional layer in depth as illustrated in Fig. 2. The individual clusters that make up these low-level/high-level pairings are further characterized by the number of layers represented (four or five layers; 4L and 5L respectively), as well as the Si_xH_y stoichiometry of silicon atoms and cluster-terminating hydrogen atoms.

One technical detail to note is that the cluster-terminating hydrogen atoms in all our cluster models are held fixed during geometry optimization. This is done to emulate the strain imposed by the surrounding surface and bulk atoms that are not explicitly represented by the cluster model. The same constraints are applied when vibrational frequencies are calculated. The constrained positions of the cluster-terminating hydrogen atoms are defined using a relaxed periodic-slab model of the Si(001) surface as a "surface structure template" (see Ref. 49 for details of the computational model that was used to obtain this slab model). This structure template is composed of 25 atomic layers of silicon and is terminated on both sides with a (2×1) monohydride surface reconstruction (i.e. H-Si-Si-H dimers; see note in Ref. 61). The cluster-terminating hydrogen atoms for a given cluster size (e.g. the 3D2R4L $Si_{49}H_{40}$ cluster) are derived from this structure template by (1) identifying all the Si-Si bonds that are broken when the Si atoms of the cluster are "extracted" from the template, and (2) placing hydrogen atoms along the direction of the broken bond such that the bond length between the extracted cluster Si atom and the hydrogen atom is 1.49 Å. The hydrogen atom positions obtained by this procedure are used as constrained positions in all

subsequent optimizations for this cluster. The procedure is described and motivated in detail in Ref. 49 (and, similarly, in Ref. 62). The more general effects of cluster size on calculated adsorption energies have been exhaustively explored in Ref. 62.

Method	PH_3 (**A1**)	PH_2+H (**B1**)	PH+2H **(C1)**	Reference
B3LYP, CCM (2D1R)	-0.69	-2.03	-2.91	This work
B3LYP, CCM (3D1R)	-0.65	-2.01	-2.86	This work
B3LYP, CCM (3D2R)	-0.68	-1.99	-2.86	This work
B3LYP, $Si_{21}H_{20}$ cluster	-0.89	-2.29	-3.38	Ref. 17
BLYP-GGA, (8x8) slab	-0.58	-1.88	-2.75	Ref. 17
PW91-GGA, (2x4) slab	-0.90	-2.04	-2.94	Ref. 26
PBE-GGA, (2x2) slab	-0.56	-2.25	-	Ref. 23
Experiment	-	-1.8	-	via Ref. 6

Table 2: Comparison of adsorption energies (in eV) of dative PH_3 (structure **A1**), on-dimer PH_2+H (structure **B1**), and centered PH+2H (structure **C1**) as calculated using the three different cluster composite models (CCM), namely 2D1R, 3D1R, and 3D2R, and earlier results in the literature. The experimental adsorption energy of approximately -1.8 eV was estimated using the Redhead equation [63] from temperature-programmed desorption data reported by Colaianni et al. [6], namely a peak desorption temperature of 635 K and a heating rate of 2 K/s, and using a attempt frequency of 10^{13} s^{-1}.

In order to illustrate the performance of this method, we give in Table 2 an overview of adsorption energies calculated for three structures that are key to the discussion, namely dative PH_3, on-dimer PH_2+H, and centered PH+2H. The table compares results obtained using our cluster composite model for the three types of cluster pairings 2D1R, 3D1R, and 3D2R described above. Also included in this comparison are energies reported in the theory literature, as well as one experimental value for PH_2+H [6]. The data in Table 2 shows good numerical agreement between the three cluster pairing models. Differences in the energies between cluster pairings of up to 0.05 eV illustrate the extent to which residual cluster size effects still affect the energetics. For our purposes, these errors are small enough so that results from different cluster pairing models can be discussed in combination. The agreement of our results with earlier publications [17, 23, 26] is also good, taking into account that these works differ considerably from ours in terms of methodology. We note specifically that

the adsorption energies reported in our earlier B3LYP cluster calculations [17] are systematically more negative. This is primarily due to the smaller basis set used in Ref. 17.

Transition state geometries were computed using the synchronous transit-guided quasi-Newton method of Peng and Schlegel [64] as implemented in the Gaussian 09 software [48]. This method is applied to all terms of the cluster composite model (Eq. 1), and therefore our calculated transition state energies and activation energies are fully compatible with the energies obtained for stable, local minimum energy structures. All calculated transition states are characterized as such by a single vibrational normal mode with a negative curvature on the potential energy surface. This is assessed on the basis of the harmonic vibrational frequency calculation that underpins the last term in Eq. 1. These vibrational frequency calculations are also used to estimate attempt frequencies, A, using the Vineyard equation [65]

$$A = \prod_i \upsilon_i^R / \prod_i \upsilon_i^{TS} \quad (3)$$

where $\{\nu_i^R\}$ and $\{\nu_i^{TS}\}$ are the sets of real-valued vibrational frequencies of the reactant and the transition state, respectively.

With these attempt frequencies and the calculated activation energies, we can estimate the rate of reaction, k, using the Arrhenius equation. In the following we will report reaction rates more conveniently as timescales $\tau=1/k$, which corresponds to the mean lifetime of the reacting species. Here it is useful to recall that time periods τ, $\tau/10$, and $\tau/100$ correspond to, respectively, 63%, 10%, and 1% of the reacting species having completed the reaction. We stress that the reaction rates and timescales should only be considered order-of-magnitude estimates, due to the fact that our DFT-calculated activation energies enter the Arrhenius equation via an exponential.

The Arrhenius equation also assumes the nuclear motion across the reaction barrier to be driven entirely by classical mechanics. However, quantum mechanical tunneling through the barrier can result in a considerable acceleration of the reaction rate, especially at low temperatures and for reactions that are characterized by a low reduced mass at the transition state (e.g. hydrogen shift reactions). This tunneling acceleration can be loosely estimated as a correction factor Γ^*=k(quantum mechanical)/k(classical) using a one-dimensional Eckart-potential model [66, 67], which takes as input the activation energy, the reaction energy, the temperature, as well as the reduced mass and negative harmonic force constant at the transition state. It is instructive to express this acceleration in the form of an activation energy correction, $\Delta E_{A,tunnel}$ due to tunneling, which is given by

$$\Delta E_{A,tunnel} = -k_B T \ln \Gamma^* \quad (4)$$

where the sign is defined such that a negative energy correction corresponds to an activation energy reduction. We note that all activation energies, E_A, and reaction rates, τ, in the following text correspond to the classical (uncorrected) barriers and rates. For those reactions that could experience a significant acceleration due to quantum tunneling effects, we report $\Delta E_{A,tunnel}$ separately to give a sense of the magnitude of the effect. Here it is useful to know that activation energy corrections of -0.1, -0.05, and -0.01 eV correspond to rate accelerations at 298.15 K by a factor of 49, 7.0, and 1.5, respectively.

B. Scanning Tunneling Microscopy

Experiments were performed using an Omicron variable temperature scanning tunneling microscope (STM) housed in an ultra-high vacuum (UHV) chamber with a base pressure of less than 5×10^{-11} mbar. The Si(001) surface was prepared from phosphorus doped 1 Ω·cm silicon (001) wafers as described previously [42]. The sample was outgassed overnight in vacuum at approximately 850 K using a resistive heating element. Prior to dosing, the sample was flashed to approximately 1450 K for 10 seconds by running a direct current through the sample, and then cooled slowly from approximately 1175 K to room temperature at a rate of approximately 3 K/s. Flash annealing has been shown to reduce the dopant density near the surface in degenerately n-type doped samples by approximately an order of magnitude [68] and we similarly anticipate some reduction in doping at the surface for our samples. Phosphine gas (PH_3) was contained within a micro-dosing system, which employed internally electro-polished gas lines assembled in a clean-room environment. Ultra-high purity (99.999%) PH_3 was admitted into the UHV chamber through a precision leak valve with line of sight to the sample. Mass spectra taken in the chamber during PH_3 exposure revealed no significant increase in the partial pressure of any other species. All STM images were obtained at room temperature using electrochemically etched tungsten tips. The quoted bias voltage is applied to the sample with reference to the tip at ground potential. Dual bias images were taken by applying a negative bias to the sample as the tip was scanned in the forward (left to right) direction and applying a positive bias to the sample as the tip was scanned in the reverse direction, simultaneously obtaining filled- and empty-state images of the surface. Investigation of diffusion and dissociation processes involved obtaining sequences of STM images over periods of typically 3 to 12 hours. Data acquisition rates were approximately one to three minutes per frame. The images were then examined frame-by-frame and changes to the position or appearance of any feature were recorded. Care was taken to ensure that the process of STM imaging does not significantly affect the surface chemistry. This was ascertained by comparing regions of the surface that have been imaged for long periods with other regions that have not.

III. RESULTS

A. Main Dissociation Path: From PH_3 to P+3H

Calculations of the initial adsorption and dissociation steps of a phosphine molecule on the Si(001) surface were conducted using the 2D1R cluster composite model (*cf.* Table I) that describes two dimers within the small-cluster region and includes the effects of two more dimers via the cluster size correction. The reaction steps considered are outlined in Fig. 3, wherein individual structures are labeled using a notation of letters and numbers (**A1**, **B1**, **B2**, **C1** etc.). These labels are consistent with those used to denote structures in our prior work (e.g. Refs. 16 to 18) with the letters A, B, C, D indicating structures that contain PH_3, PH_2, PH, and P adatoms, respectively. The reaction pathway discussed here improves on our previous calculations [16-18] by describing all the reaction steps from PH_3 to P+3H and using a much more reliable computational model. As we will show, this results in a description of the kinetic barriers of phosphine dissociation that is in agreement with experimental observations.

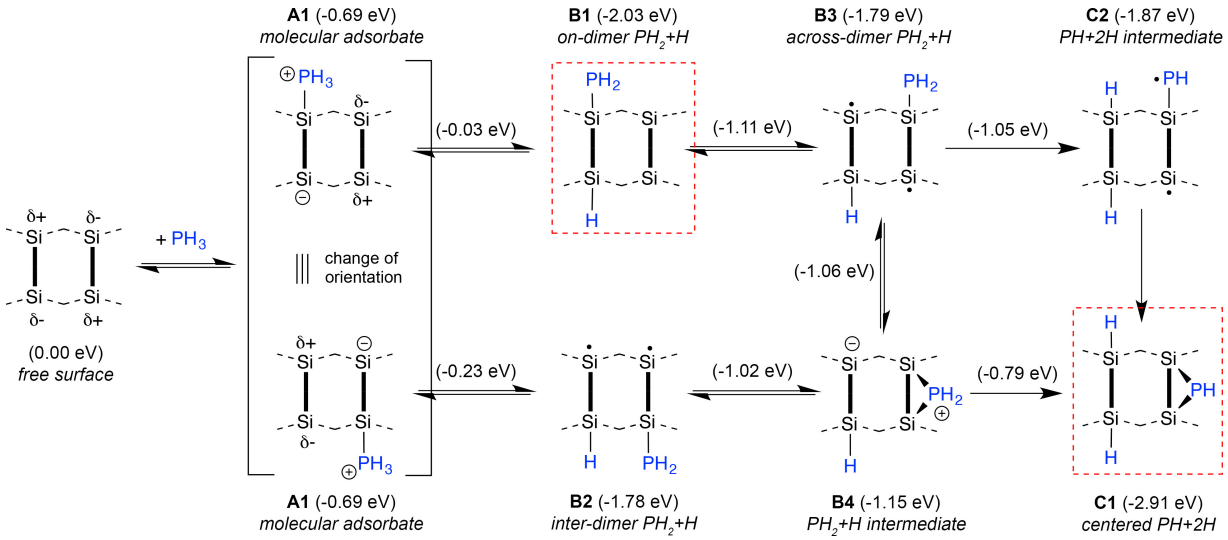

Figure 3: Schematic pathway of the adsorption and dissociation of PH_3 on the Si(001) surface, starting with the free surface on the left and leading to the centered feature PH+2H (structure **C1**) at the lower right. Shown with each structure are the calculated adsorption energies using the 2D1R cluster composite model. Also reported for every reaction arrow is the adsorption energy of the corresponding transition state. Structures enclosed by dashed (red) boxes are observed in room-temperature STM experiments (Refs. 16-18; and Fig. 5 below). All other structures are too short-lived to be observable.

Impinging on the surface, the PH_3 molecule first reacts to form the molecular adsorbate structure **A1** in which PH_3 is datively bonded to a down-buckled, electrophilic (δ^+) atom of a Si—Si dimer. The adsorption reaction is barrier-less and exothermic with an energy gain of 0.69 eV. This is in agreement with the experimentally observed sticking coefficient of

unity [2,3] and with previous theoretical studies, reporting adsorption energies of -0.56 eV [23], -0.90 eV [26], -0.89 eV, and -0.58 eV (Ref. 17; B3LYP cluster and GGA-DFT slab model, respectively).

Molecularly adsorbed PH_3 is prone to undergo deprotonation, i.e. the loss of a hydrogen atom from the PH_3 fragment leading to a variety of structures of PH_2+H composition as shown in Fig. 3. A hydrogen-shift to the opposite dimer end produces the *on-dimer* PH_2+H structure **B1**, which is the thermodynamically favored arrangement of a pair of PH_2 and H fragments on the silicon (001) surface [16,17]. The calculated adsorption energy of -2.03 eV is again in good agreement with previous theory reports for this structure of between -1.88 and -2.29 eV [17,23,26]. This energy is also in reasonable agreement with an experimental estimate of -1.8 eV, which is derived from temperature programmed desorption (TPD) experiments reported by Colaianni *et al.* (Ref. 6; see also notes given in the caption of Table 2).

Also plausible for structure **A1** is a hydrogen-shift to an adjacent dimer, which produces structure **B2** as shown in the lower branch of Fig. 3. This *inter-dimer* PH_2+H structure has a calculated energy of -1.78 eV, which is 0.25 eV less stable than on-dimer PH_2+H on account of two unpaired dangling bonds. Equilibration between on- and inter-dimer PH_2+H (structures **B1** and **B2**) occurs via shifts of the PH_2 fragment and two additional PH_2+H structures, labeled **B3** and **B4** in Fig. 3. In structure **B3** the PH_2 and H fragments are bonded to adjacent dimers, but at opposite dimer ends. Structure **B4** is an intermediate between **B2** and **B3**, in which the PH_2 fragment is positioned centered above a Si-Si dimer. This intermediate, at -1.15 eV, is the least stable of the PH_2+H configurations in this path.

The PH+2H structure **C1**, a combination of a dimer-centered PH fragment and a H-Si-Si-H monohydride, is prominently observed in STM images of a phosphine-dosed Si(001) surface [16, 17]. With a calculated energy of -2.91 eV, structure **C1** is almost 0.9 eV more stable than the preferred PH_2+H structure **B1**. Two competing paths that lead to this structure are examined in Fig. 3. We have previously proposed [18] the reaction path in Fig. 3 that involves structure **B4** as an intermediate. In this path, a hydrogen atom shifts from a dimer-centered PH_2 fragment of structure **B4** to an adjacent dimer to produce structure **C1**. Here we also consider an alternative that involves two reaction steps beginning with the across-dimer PH_2+H structure **B3**. In the first step, a hydrogen atom shifts from the PH_2 fragment of structure **B3** to the adjacent hemihydride dimer to form structure **C2** in which the remaining PH fragment is bonded to a single silicon atom at one dimer-end. In the second reaction step, the PH fragment shifts to the center of the dimer to form the three-membered ring of structure **C1**. In the kinetics discussion below, we will determine which of these two paths is preferred.

The onwards reaction of the PH+2H structure **C1** involves a third Si-Si dimer, which requires that we use the larger 3D1R cluster composite model. Figure 4 outlines the two reaction steps that lead to the end-bridge P+3H structure **D2**, which we have assigned to an experimentally observed feature in room temperature STM experiments [16,17]. In the first reaction step, the dimer-centered PH fragment shifts its remaining hydrogen atom onto the third dimer producing the P+3H structure **D3** with a dimer-centered phosphorus adatom. The second step occurs because phosphorus adatoms tend to prefer the end-bridge position between two dimer ends [28]. Accordingly, the dimer-bridge structure **D3** rearranges to the end-bridge structure **D2**, gaining 0.40 eV in the process. Overall, structure **D2** is slightly (0.17 eV) more stable than structure **C1**.

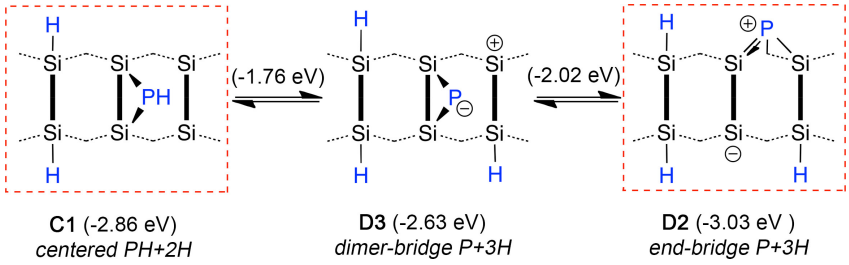

FIG. 4: Reaction steps from the PH+2H structure **C1** to the end-bridge P+3H structure **D2**. Adsorption energies are reported with each structure and were calculated using the 3D1R cluster composite model. Also reported for every reaction arrow is the adsorption energy of the corresponding transition state. Structures **C1** and **D2** are enclosed by dashed (red) boxes to indicate that both are observed in room-temperature STM experiments (Refs. 16-18; and Fig. 5 below). The intermediate structure **D3** is short-lived and not observed in experiment.

B. Main Dissociation Path – Calculated Kinetics vs Experiment

Figure 5(a-c) is an example of how the room-temperature dissociation of phosphine is observed in STM experiments. In the center of the three images a phosphine-related adsorbate can be seen to undergo a sequence of drastic changes in appearance due to chemical reactions that occur. In previous work [16,17] we have assigned the three adsorbate species involved in these reactions to PH_2+H (structure **B1**), PH+2H (structure **C1**), and P+3H (structure **D2**). The correspondence between the chemical structure of these species and their STM appearance is illustrated using schematic valence structure diagrams in Fig. 5(d-f). This constitutes what we refer to here as the PH_3 *main dissociation sequence*.

Using transition state calculations we will now describe how these three species arise in STM experiments. Transition state optimizations have been carried out for each of the reaction steps in Figs. 3 and 4, and the energies of the structures obtained are combined with those of the minimum energy structures. From this data we construct the schematic potential energy diagram that is shown in Fig. 5(g) in which all structures along the pathways of Fig. 3 and 4 are represented by thick, black horizontal bars. All stable (minimum energy) structures are labeled with the corresponding structure label

(**A1**, **B1**, **B2**, etc.) and transition states are marked using an asterisk (*). Overall we observe in Fig. 5(g) a progressive gain in stability from left to right as the phosphine adsorbate transfers hydrogen atoms from phosphorus to silicon as it goes through the four stages PH_3 (structure **A1**), PH_2+H (structure **B1**), PH+2H (structure **C1**), and P+3H (structure **D2**).

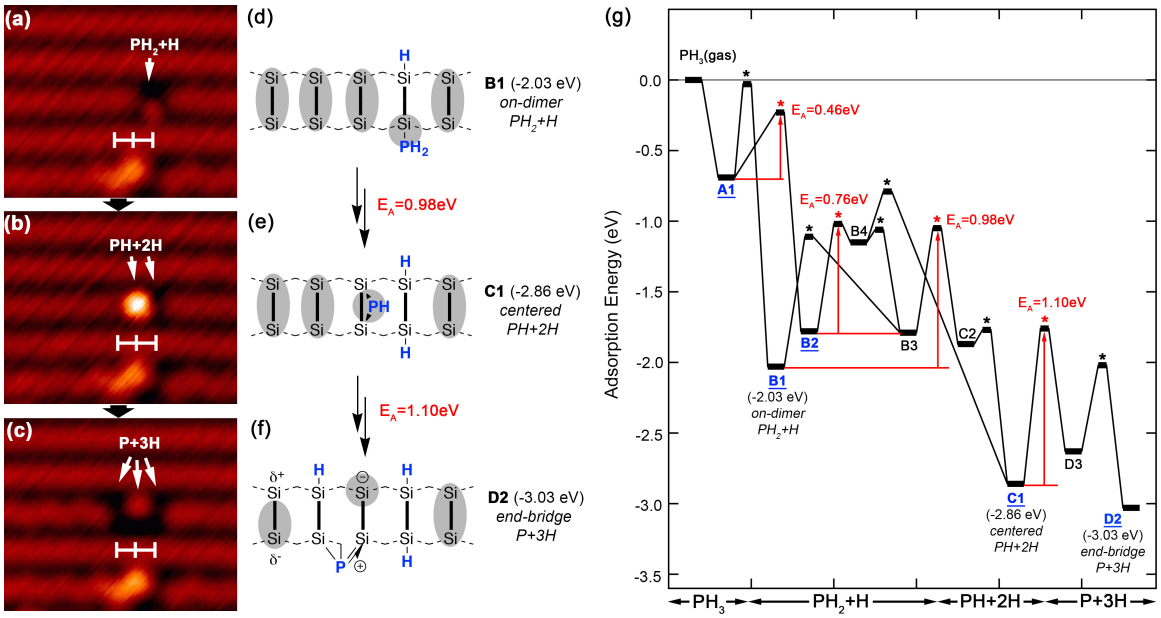

FIG. 5: The PH_3 main dissociation sequence. (a-c) Three filled-state STM images (sample bias -2 V) recorded in sequence show the dissociation of on-dimer PH_2+H into PH+2H and then P+3H. A nearby dimer vacancy plus hemihydride defect provide a reference for the relative alignment of the three images. Panels (d)-(f) show the corresponding valence structure schematics of the species seen with the imaging sites highlighted with grey shading. (g) Calculated potential energy diagram illustrating the energetics of the main dissociation sequence. Minimum energy and transition state structures are represented using thick horizontal bars. Transition states are further marked using an asterisk (*). Five key intermediate structures (**A1**, **B2**, **B1**, **C1**, **D2**) and the rate-determining activation barriers between them are indicated using blue-colored labels and red-colored arrows, respectively. Note that the PH_2+H and P+3H features in (a) and (c) differ in being one and three dimers wide, respectively. These features are more clearly distinguished in empty-state STM images (not shown here, but see e.g. Ref. 16). Note that the adsorption and activation energies reported in panels (d-g) are a combination of results obtained using the 2D1R and 3D1R cluster composite models.

The kinetics of PH_3 dissociation and the rates of reaction are determined by the activation energies. While all reaction steps are included in Fig. 5(g), the overall kinetics is best appreciated by focusing on a subset of five key structures, namely **A1**, **B1**, **B2, C1** and **D2** [these labels are colored blue in Fig. 5(g)]. The four effective (multistep) activation energies between these five structures govern the dissociation process, and they have been highlighted in Fig. 5(g) using red-colored arrows. Key numerical details of these transitions are summarized in Table 3.

In Figure 5(g), the highlighted activation energy of E_A=0.46 eV governs the dissociation of the molecularly adsorbed PH_3 species **A1** into a PH_2+H species. The structure that results from this transition is the inter-dimer PH_2+H structure **B2** in which the two fragments PH_2 and H are bound to adjacent dimers. The reaction barrier is small enough to be easily crossed at

room temperature. Combined with a calculated attempt frequency of 4.7×10^{12} s^{-1} (see Table 3) we can estimate the Arrhenius timescale of this reaction to be in the order of 10 μs at room temperature. This timescale is further reduced by factor of approximately four if an effective barrier correction, $\Delta E_{A,tunnel}$, of -0.04 eV (Eq. 4 and Table 3) due to quantum tunneling is taken into account. Hence, the molecular adsorbate is short-lived, and not observable in our room temperature STM experiments where single images are recorded on a timescale of minutes, and repeated image sequences are acquired over periods of minutes to hours. We note that Maity *et al.* [8] have explored the energetics of this particular reaction barrier using supersonic molecular beam experiments, which placed the transition state of the PH_3 to PH_2+H surface reaction at 8.6 kcal/mol (0.37 eV) below the dissociation limit. This is in reasonable agreement with our calculations, where the transition state is at 0.23 eV below the limit.

	$\Delta_R E$ (eV)	E_A (eV)	A (s^{-1})	τ	$\Delta E_{A,tunnel}$ (eV)
A1 (PH_3) → **B2** (PH_2+H)	-1.09	0.46	4.7×10^{12}	12 μs	-0.04
B2 (PH_2+H) → **B1** (PH_2+H)	-0.26	0.76	6.0×10^{12}	1 s	0.00
B1 (PH_2+H) → **C1** (P+2H)	-0.87	0.98	3.8×10^{12}	3 h	-0.08
C1 (PH+2H) → **D2** (P+3H)	-0.17	1.10	1.9×10^{13}	62 h	-0.03

Table 3: Calculated reaction energies, $\Delta_R E$, activation energies, E_A, and attempt frequencies, A, for the four critical transitions highlighted in Fig. 5(g). Also included in the table is the reaction timescales, τ, of the reaction at 298.15 K which is calculated as the inverse of the Arrhenius rate. An approximate activation energy correction, $\Delta E_{A,tunnel}$ (also at 298.15 K; see Eq. 4) based on an Eckart-potential model quantifies the possible effect of quantum tunneling on the activation energy. All but the **A1→B2** process involve multiple reaction steps for which the activation energies, attempt frequencies, and tunneling corrections were calculated using the rate-determining (i.e. highest energy) transition state along the multistep path. All energies and attempt frequencies were obtained using the 2D1R cluster composite model, except the **C1→D2** process for which the 3D1R model was used.

Structure **B2** is able to convert to the more stable structure **B1** via the multistep path **B2→B4→B3→B1** [see Fig. 3]. The rate of this conversion is determined by the highlighted activation energy of E_A=0.76 eV in Fig. 5(g). Again, this activation energy is small enough at room temperature to be rapidly crossed with a timescale of about one second (see Table 3). Due to the larger mass of the migrating PH_2 fragment, this timescale is not significantly affected by quantum tunneling effects. We can therefore conclude that none of structures **B2**, **B3**, and **B4** is long-lived enough to be directly observable in our room temperature STM experiments.

In contrast, on-dimer PH_2+H (**B1)** is observable in room temperature STM experiments. This is because of the activation energy highlighted in Fig. 5(g) of E_A=0.98 eV, which determines its rate of dissociation. This barrier takes structure **B1** via intermediates **B3** and **C2** to the significantly more stable PH+2H structure **C1**. The calculated Arrhenius timescale, τ, of this reaction of approximately 3 hours (Table 3) is large enough to give an observable rate of reaction at STM imaging timescales. Indeed, the characteristically asymmetric protrusions that we identify as structure **B1** are seen to convert in STM imaging sequences into bright protrusions centered on the dimer row. Figure 5(a) to (b) is an example of such a transition. We note that the rate-determining step in this transition is the hydrogen-shift reaction between **B3** and **C2**, which can be expected to experience some acceleration due to quantum tunneling. A simple estimate of the effective barrier correction due to quantum tunneling gives a value of $\Delta E_{A,tunnel}$=-0.08 eV at 298.16 K, which would correspond to a significant rate acceleration by a factor of 21 (or a corrected timescale of 9 minutes). This acceleration, however, is likely to be a significant overcorrection because not all the reaction steps between **B1** and **C1** benefit from the low transition mass of the **B3** to **C2** hydrogen-shift. In fact, the first step in the multistep **B1** to **C1** transition, namely the PH_2-shift between **B1** and **B3** is almost rate determining, with an activation energy of 0.93 eV and a quantum tunneling correction that is negligible. Therefore, the **B1** to **B3** reaction step is likely to limit the effect of the **B3** to **C2** tunneling acceleration on the overall rate of reaction between **B1** and **C1**.

The PH+2H structure **C1** in turn converts into a three dimer-wide STM feature, which has been described as having a distinct U-shaped appearance [23, 24, 25]. An example of such a transition is shown in Fig. 5(b) to (c). This three-dimer species can be explained by the P+3H structure **D2** [23, 24], which is 0.17 eV more stable than **C1**. The highlighted activation energy in Fig. 5(g) of E_A=1.10 eV is rate-determining for this transition. Due to the somewhat larger barrier, this transition is predicted to be slower than the prior **B1** to **C1** transition. The calculated timescale is τ=62 hours (see Table 3). Considering a more practical experimental timeframe of 37 minutes (i.e. τ/100), the prediction is that 1% of PH_2+H would has converted to P+3H. The rate-determining reaction step of the **C1** to **D2** transition is again a hydrogen-shift, which means there could be some acceleration of this process by quantum tunneling effects. The calculated tunneling correction of $\Delta E_{A,tunnel}$=-0.03 eV at 298.16 K corresponds to a predicted acceleration of the **C1** to **D2** transition by a factor of 3.3, or a reduction of the reaction timescale from 62 hours to 19 hours.

There are two alternative pathways in Fig. 3 that lead to structures **B1** (PH_2+H) and **C1** (PH+2H); both are unfavorable on kinetic grounds, as we will now describe. The first of these alternatives is the direct, one-step reaction from

the molecular adsorbate **A1** to the on-dimer PH_2+H structure **B1** by way of an on-dimer hydrogen shift. The activation energy for the on-dimer shift computes to E_A=0.66 eV, which cannot compete with the E_A=0.46 eV barrier of the inter-dimer shift (**A1→B2**). Using the calculated rates of reaction we estimate that the inter-dimer process is faster by a factor of approximately 2000. This factor increases to approximately 3000, with the inclusion of Eckart quantum tunneling effects. We can therefore conclude that the vast majority of on-dimer PH_2+H adsorbates are formed by the more circuitous inter-dimer route **A1→B2→B4→B3→B1** (see Fig. 3). The second alternative pathway commences with structure **B1** (PH_2+H) and leads to structure **C1** (PH+2H) via structure **B4** instead of **C2** as discussed above. The effective barrier for this pathway is E_A=1.24 eV, which cannot compete with the effective barrier of E_A=0.98 eV for the path via structure **C2**. A comparison of the calculated Arrhenius reaction rates predicts that the pathway via structure **C2** (i.e. **B1→B3→C2→C1**) is very much faster ($k_{via\text{-}C2}/k_{via\text{-}B4}$~60000). Moreover, quantum tunneling is predicted to be much more effective for the pathway via structure **C2** ($\Delta E_{A,tunnel}$=-0.08 eV), which further disadvantages the alternative path via **B4** ($\Delta E_{A,tunnel}$=-0.01 eV).

This concludes our results for what we refer to as the *main dissociation sequence* observed in STM experiments, with our theoretical calculations explaining how the observed asymmetric PH_2+H, centered PH+2H, and U-shaped P+3H STM features are formed. We will now focus on several additional, less common surface species that arise from alternative reaction processes. As we will describe, these processes can be understood by analogy to the main sequence, allowing us to arrive at a more complete picture of the PH_3/Si(001) surface chemistry.

C. Inter-row Dissociation of the Phosphine Adsorbate

In the context of the main sequence, we have discussed the dissociation of molecularly adsorbed PH_3 (structure **A1**) undergoing a hydrogen-shift reaction along on-dimer and inter-dimer directions to produce PH_2+H structures **B1** and **B2**, respectively (*cf.* pathways in Fig. 3). There are however several important reactions by which parts of an adsorbed phosphine molecule are transferred from one dimer-row to the next. Shown in Fig. 6 is the same type of hydrogen-shift dissociation going in an inter-row direction, that is, a hydrogen atom from a PH_3 adsorbate [Fig. 6(a)] is transferred across to an adjacent row [Fig. 6(b)] to produce inter-row PH_2+H [Fig. 6(c)]. The process is exothermic with a reaction energy of -0.98 eV as calculated using the 3D2R composite model. The activation energy computes to E_A=0.47 eV, which is surprisingly competitive with that of the inter-dimer process (**A1** to **B2**) of 0.46 eV, and much preferred over the on-dimer process (**A1** to **B1**) of 0.65 eV. The inclusion of quantum tunneling effects does not change this qualitative finding with all three processes (inter-row, inter-dimer, and on-dimer) experiencing very similar barrier corrections, $\Delta E_{A,tunnel}$ (Eq. 4), in the range of -0.04

and -0.03 eV at 298.15 K. Therefore, we should expect a fraction of adsorbing phosphine molecules to break up across two dimer rows. Those molecules that break up on the same row will immediately react to the on-dimer **B1** structure, as discussed above, and eventually progress further through the main dissociation sequence. In contrast, phosphine molecules that are split across two dimer rows will undergo a quite different set of transformations. Before we can further discuss these transformations, we need to engage with the topic of PH_2 diffusion.

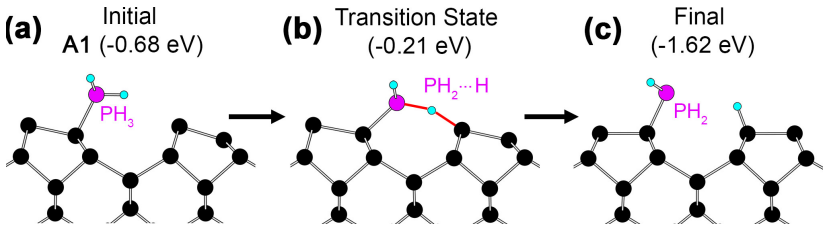

FIG. 6: The break up of molecularly adsorbed PH_3 (structure **A1**) by an inter-row hydrogen shift to produce inter-row dissociated PH_2+H. The calculated activation energy, E_A, of this process is 0.47 eV, which is competitive with the inter-dimer H-shift reaction (E_A=0.46 eV) of the main dissociation sequence (Fig. 5). The Eckart-model quantum-tunneling correction, $\Delta E_{A,tunnel}$ (see Eq. 4) to the activation energy for this reaction is calculated to be -0.03 eV at 298.15 K, which is also comparable to that of the inter-dimer H-shift reaction (-0.04 eV). Panels (a), (b), and (c) give a side view of the initial structure, the transition state, and the final structure, respectively. Note that in this orthographic view, two of the PH_x hydrogen atoms are aligned, one directly behind the other, and thus appear as one atom. Silicon, phosphorus, and hydrogen atoms are colored black, purple, and light blue, respectively. The covalent bonds that form and break in the transition state are highlighted in red. The energies and structures shown were calculated using the 3D2R cluster composite model.

D. PH_2 Diffusion

As we demonstrate in this section, the diffusion of PH_2 plays a surprisingly important role in the chemistry of phosphine on the silicon (001) surface. We have already seen in the main dissociation sequence (Fig. 3) that PH_2 fragments can readily shift between neighboring dimers. The barriers involved are small (E_A=0.76 eV: see Table 3) which results in the rapid conversion of the PH_2+H structures **B2**, **B3**, and **B4** into the preferred on-dimer configuration **B1**. Note, however, that the reverse barriers from **B1** into **B2** to **B4** of between 0.92 and 1.01 eV remain accessible at room temperature. As a result, the PH_2 fragment in structure **B1** can be expected to undertake occasional short-lived excursions to the dimers adjacent to the hydrogenated dimer. The energetics also suggests that PH_2 fragments could stray even further away. For two fully separated PH_2 and H fragments, the adsorption energy evaluates to -1.72 eV. This is very slightly less stable than adjacent-dimer PH_2+H (structures **B2** and **B3**; -1.78 and -1.79 eV, respectively), but still within a plausible range from the on-dimer PH_2+H configuration (**B1**; -2.03 eV).

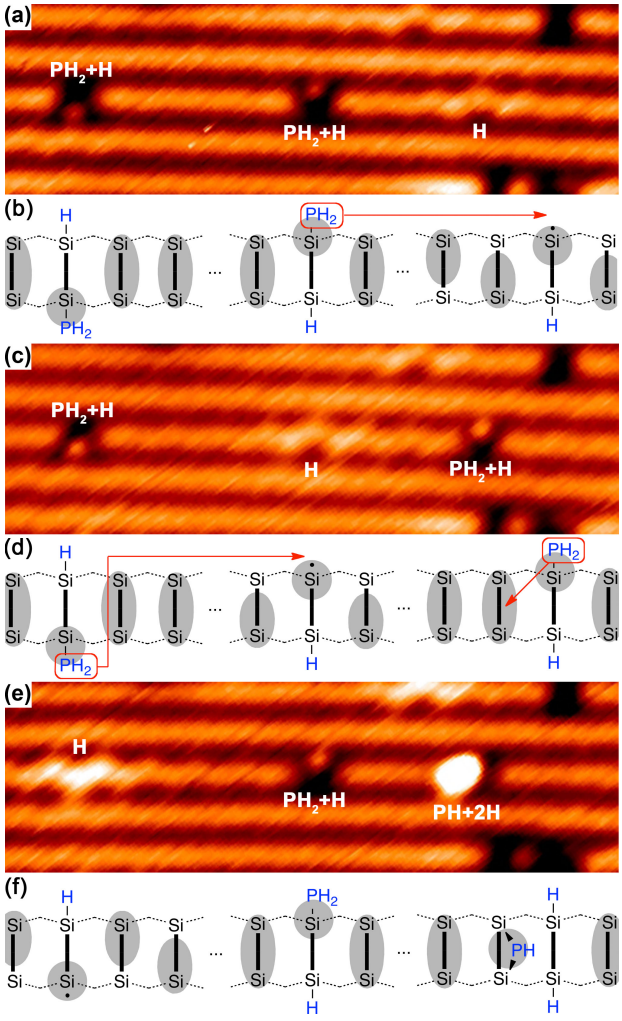

FIG. 7: Example of PH_2 diffusion events as seen in STM image sequences. (**a**), (**c**) and (**e**) show the same 5 dimer rows, taken from a sequence of 36 scans after PH_3 dosing, obtained with sample biases of -1.1, -1.2 and -1.7 V, respectively. The schematics show segments of the central dimer row where the features are located. The arrows indicate the diffusion events (PH_2+H) + H → H + (PH_2+H) in (b) and (d) and the dissociation event PH_2+H → PH + 2H in (d). The three STM images were recorded 37, 54 and 57 minutes after the initial PH_3 dose.

Experimentally, such PH_2 excursions are not directly observable in room temperature STM images, because they are short lived (milliseconds) in comparison to the time it takes to record an image (minutes). However, they can be inferred from image sequences where on-dimer PH_2+H asymmetric features and hemihydride dimers are in close proximity. In these cases, the PH_2 fragment may not recombine with the hydrogenated dimer from which it originated, but can instead shuttle over to the nearby hemihydride and form a long-lived, observable PH_2+H feature.

In STM image sequences (see Fig. 7) this reaction is observed as an apparent switching of asymmetric PH_2+H and hemihydride H features in successive images. In the first image shown [Fig. 7(a)] three distinct adsorbates are seen on a single dimer row. Going from left to right, these are: PH_2+H, PH_2+H and H. Figure 7(b) illustrates the PH_2 shuttling process

that gives rise to the second STM image in this sequence, Fig. 7(c). A PH_2 fragment migrates from the middle feature to the right; hence, between Figs. 7(a) and (c), the middle feature changes from a PH_2+H to H, while the feature on the right changes from H to PH_2+H. Further diffusion and dissociation events are outlined in Fig. 7(d) that result in the final configuration shown in Figs. 7(e) and (f): H, PH_2+H, and PH+2H. A PH_2 fragment migrates from the feature on left to the middle feature, hence these PH_2+H and H features appear to switch positions between Fig. 7(c) and (e). The PH_2+H feature on the right in Fig. 7(c) has dissociated into a bright centered PH+2H species in Fig. 7(e).

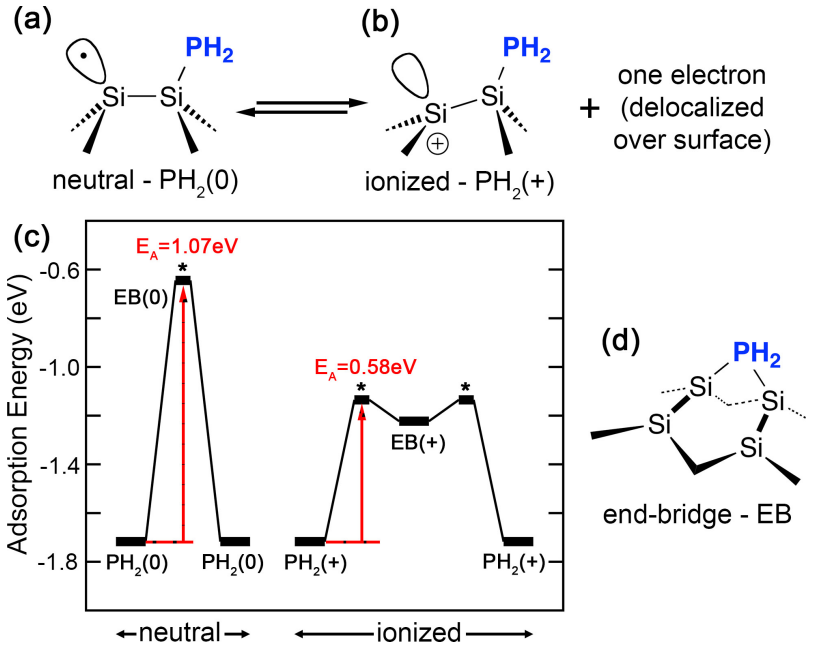

FIG. 8: (a) Neutral and (b) positive charge states of a diffusing PH_2 fragment on the silicon (001) surface. The schematics illustrate how these two charge states differ primarily in the occupancy of the dangling bond orbital at the opposite dimer end. The potential energy profile of inter-dimer PH_2 diffusion for neutral and positive charge states is sketched out in panel (c) in which local minimum energy structures and transition states are represented using long and short horizontal bars, respectively. Transition states are further indicated using an asterisk (*). The (free) energy alignment between the two charge states assumes that $PH_2(0)$ and $PH_2(+)$ fragments are in equilibrium, that is the PH_2 fragment can spontaneously ionize and utilize the lower-barrier $PH_2(+)$ diffusion profile. Illustrated in (d) is the symmetric end-bridge (EB) configuration that the PH_2 fragment passes through when diffusing from one dimer to the next. This configuration is a transition state in the $PH_2(0)$ diffusion process and a shallow intermediate in the $PH_2(+)$ process.

The most instructive aspect of these images is what they reveal about the nature of the PH_2 diffusion process. Here the critical point is that the PH_2 species is nominally an odd-electron species, when separated from its H counterpart, and as such is prone to undergo localized charging on the silicon surface. As illustrated in Fig. 8(a), the odd electron nominally occupies the dangling bond of the half-terminated Si-Si-PH_2 dimer. However, as previously shown for the electronically analogous Si-Si-H hemihydride [69-72] and other defects [73-75], such half-terminated dimers with singly occupied dangling bonds are easily ionized; i.e. the odd electron is delocalized away from the dangling bond into a highly dispersed surface

conduction band. Because such a delocalized electron has a low probability of residing in the vicinity of the Si-Si-PH_2 dimer, this dimer in effect adopts a locally positive charge state with a dangling bond orbital that is unoccupied [see illustration in Fig. 8(b)]. As we will show now, a plausible interpretation of the diffusion processes in Fig. 7 requires that isolated PH_2 fragments adopt such a positive charge state.

	$PH_2(0)$	$PH_2(+)$
inter-dimer diffusion	1.07 eV (160 h)	0.58 eV (21 ms)
inter-row diffusion	1.41 eV (12000 yrs)	0.80 eV (36 s)

Table 4: Calculated activation energies (in eV) as a function of the local charge state (neutral or positive) of an isolated PH_2 fragment shifting between two dimers on the same dimer row (inter-dimer diffusion), and between two dimers on adjacent dimer rows (inter-row diffusion). Also reported are the calculated reaction timescales, τ at room temperature (in brackets). Inter-dimer diffusion barriers were calculated using the 2D1R cluster composite model, while inter-row barriers were calculated using the 3D2R model. The Eckart-model activation energy corrections, $\Delta E_{A,tunnel}$ (see Eq. 4) for these reactions is less than 5 meV in magnitude at 298.15 K, which suggests that PH_2 diffusion reactions are not significantly affected by quantum tunneling effects.

Given in Table 4 are calculated activation energies of diffusion for a PH_2 fragment in neutral and positive charge states [these are denoted $PH_2(0)$ and $PH_2(+)$ in the following]. The positive state is represented in our cluster models by the removal of an electron relative to the nominal count (see note in Ref. 76). The calculated inter-dimer barriers in Table 4 for diffusion along the dimer row has an activation energy of 1.07 eV for neutral PH_2, whereas PH_2 in a positive charge state has a much-reduced barrier of 0.58 eV. Also included in Table 4 are calculated reaction timescales, τ, for these reactions. These timescales show that the positive charge state with an inverse rate constant τ of 21 ms is consistent with rapid, random-walk diffusion over several dimers on a timescale of minutes as observed in Fig. 7. In contrast, the neutral charge state with τ=160 hours is not. In Fig. 8(c), the schematic potential energy profiles of $PH_2(0)$ and $PH_2(+)$ inter-dimer diffusion are plotted next to one another in which the energies for the positive charge state are shifted such that the ground state $PH_2(+)$ configuration is aligned with that of $PH_2(0)$. This comparison graphically illustrates the preference for PH_2 diffusion in the positive charge state. A contributing factor to the lowered barrier could be the end-bridge (EB) configuration [Fig. 8(d)] in which the diffusing PH_2 fragment is covalently bonded to two adjacent dimer ends. This configuration is a transition state in the neutral charge state [i.e. EB(0) in Fig. 8(c)] and a meta-stable intermediate in the positive charge state [EB(+)]. The somewhat *ad hoc* alignment of $PH_2(0)$ and $PH_2(+)$ ground state energies that underpins this comparison is justified if these energies are considered to be free energies in contact with a suitable electron reservoir. This electron reservoir is represented by a

chemical potential, which in the case of a surface is given by the Fermi level. The fact that dangling bond species such as Si-Si-H [69-72] and Si-P [73-75] spontaneously ionize on Si(001) suggests that the Fermi level is such that the free energy of single dangling bond species in a positive charge state is at least as stable as those in a neutral charge state.

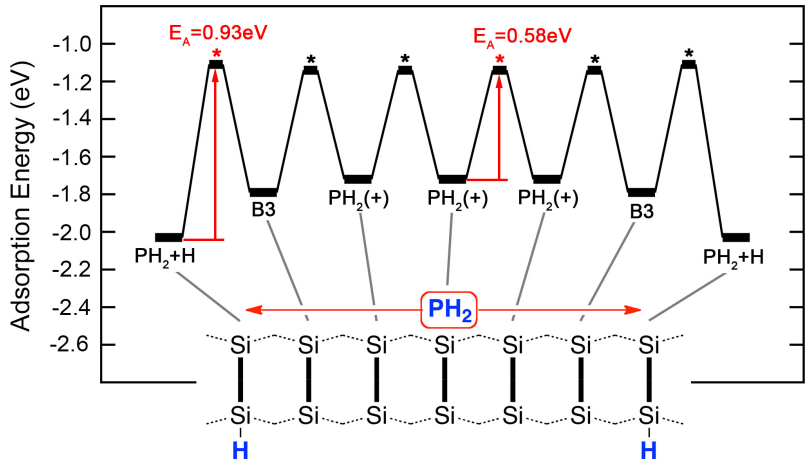

FIG. 9: Composite potential energy profile illustrating the energetics of PH_2 transfer between two hemihydride dimers, i.e. the type of switching processes described in Fig. 7. This profile combines the energies of (neutral) structures **B1** (PH_2+H) and **B3,** and the transition state between them, with the energies of isolated PH_2 diffusing in positive charge state [PH_2(+)]. The alignment assumes a PH_2 ionization energy of 0 eV; i.e. a migrating PH_2 fragment can adopt a positive charge state without energy loss or gain. Stable, local minimum energy structures and transition states are represented using a thick horizontal bar. Transition states are further indicated using an asterisk (*) symbol. All energies were computed using the 2D1R composite model.

Figure 9 illustrates the overall energetics of the exchange of a PH_2 fragment between two hemihydride dimers. The calculated energy is shown for the PH_2 fragment binding to each of the seven dimer ends as well as the transition states between these configurations. On the far right and far left, when PH_2 attaches to a hemihydride dimer, the adsorption energy is that of a PH_2+H fragment (structure **B1**; *cf.* Fig. 3), -2.03 eV. Moving the PH_2 fragment over to the adjacent dimer produces structure **B3** (*cf.* Fig. 3) with an adsorption energy of -1.79 eV. The activation energy for this shift is E_A=0.93 eV. After moving the PH_2 fragment one dimer further away from hemihydride dimer, we assume the H and PH_2 fragments to be fully separated from one another, and hence the adsorption energy becomes that of an isolated hemihydride and an isolated PH_2 fragment. This energy evaluates to -1.72 eV, which is 0.31 and 0.07 eV less stable than structures **B1** and structure **B3**, respectively. Assuming further that isolated PH_2(0) is in equilibrium with PH_2(+) means that the effective barrier from dimer to dimer is the more favorable value of 0.58 eV associated with PH_2(+). Relative to the PH_2+H configuration, this barrier becomes 0.90 eV. Hence it is barriers of about 0.9 eV that determine the net rate of PH_2 exchange between nearby hemihydrides. Using calculated attempt frequencies for these barriers, we can estimate the time constant τ at room

temperature to be approximately one hour. This time scale is qualitatively consistent with the rate of switching observed in the experimental images (Fig. 7).

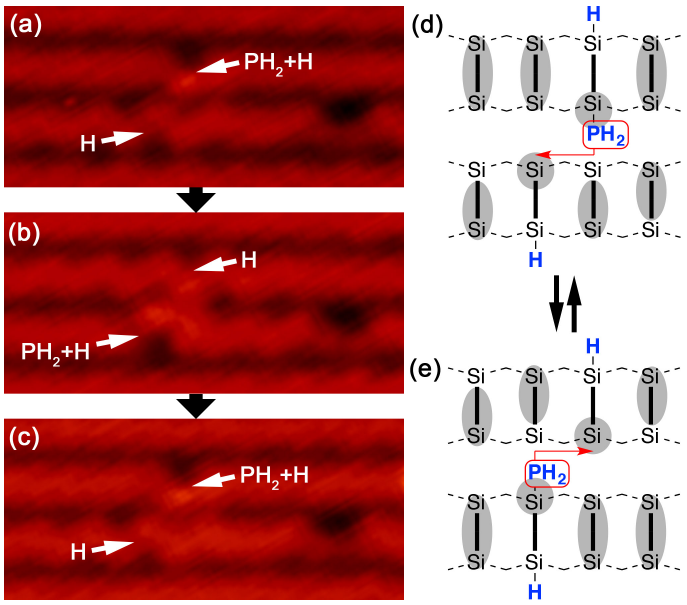

FIG. 10: A sequence of three filled-state STM images showing two inter-row PH_2 diffusion events. A PH_2+H asymmetric feature and a hemihydride dimer (H) in the upper and lower dimer row in panels (a) and (c) appear to have switched places in panel (b). The schematic valence structure diagrams in panels (d) and (e) illustrate the reversible PH_2 shift reaction across the dimer row that gives rise to this image sequence. The three STM images in panels (a-c) were previously published in Ref. 18 and were recorded using a sample bias of -2 V and a tunneling current of 0.2 nA.

STM images in Fig. 10 show that the exchange of PH_2 fragments between nearby hemihydrides can also occur when the hemihydrides are located on adjacent dimer rows. These images are adapted from images previously published in Ref. 18. Similar to the intra-row sequence above (Fig. 7), PH_2+H features and hemihydride features appear to switch places in Figs. 10(a-c), except that the switch occurs across the trough between two dimer rows. This indicates that facile diffusion mechanisms exist to transfer PH_2 fragments from one dimer row to the next.

Calculated inter-row diffusion barriers for an isolated PH_2 fragment in neutral and positive charge states are included in Table 4. Analogous to inter-dimer diffusion, we find that the inter-row activation energy in the neutral charge state of 1.41 eV is prohibitively high at room temperature to be compatible with observation. However, for PH_2 in a positive charge state, the barrier is again significantly reduced to 0.80 eV for an inter-row shift. This is an activation energy that can be crossed by an isolated PH_2 fragment at room temperature. However, as an explanation for the inter-row processes seen in Fig. 10(a-c) we need to keep in mind that these processes commence with a PH_2+H species. This raises the effective barrier of a PH_2 fragment separating from PH_2+H, and diffusing away, by a further 0.31 eV to 1.11 eV in order to account for the energy

difference between PH_2+H and fully separated PH_2 and H fragments. It thus appears improbable that the inter-row PH_2 shift occurs subsequent to an on-row separation of PH_2+H. Instead, we propose that inter-row PH_2 diffusion commences directly with the PH_2+H species.

Shown in Fig. 11 are side views of the initial structure [Fig. 11(a)], the transition state [Fig. 11(b)], and the final structure [Fig. 11(c)] of the break up of an on-dimer PH_2+H species (structure **B1**) into separated PH_2 and H fragments on adjacent rows. The calculated activation energy for this process is 0.98 eV, which is more plausible for the observed transition in Fig. 10. The transition itself is endothermic, that is, the final structure, inter-row PH_2+H, is 0.31 eV less stable than on-dimer PH_2+H. This means that the reaction back to on-dimer PH_2+H is much faster with a barrier of only 0.67 eV; however, this back reaction is in competition with the inter-dimer PH_2(+) diffusion barrier of 0.58 eV. In this situation it is more likely that the PH_2 fragment will undertake a number of random-walk diffusion steps along the dimer row, taking it away from its original hydrogen counterpart. If the diffusing PH_2 fragment encounters another hemihydride dimer along the row, a stable, observable on-dimer PH_2+H species is formed. This is exactly what is observed in the Fig. 10(a) to (b) image sequence, and then again in the reverse direction in Fig. 10(b) to (c). If, however, no such stabilization of the diffusing PH_2 fragment occurs, the back reaction, Fig. 11(c) to (a), will occur; i.e., PH_2 will return back to the row it came from and recombine with the hemihydride that the PH_2 fragment was originally paired with.

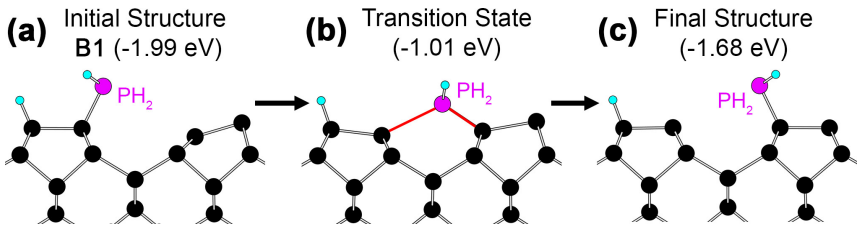

Figure 11: The break up of an on-dimer PH_2+H species (structure **B1)** by an inter-row shift of the PH_2 fragment. Orthographic side-on views of (a) the initial structure, (b) the transition state, and (c) the final structure are shown. Note that in this view the two hydrogen atoms of the migrating PH_2 fragment are aligned one behind the other, and thus appear as one atom. Silicon, phosphorus, and hydrogen atoms are colored black, purple, and light blue, respectively. The covalent bonds that form and break in the transition state are highlighted in red. The energies reported with each structure were calculated using the 3D2R cluster composite model.

E. Dissociation of a diffusing PH_2 fragment

In the previous two sections we have identified three distinct processes by which PH_2 fragments become spatially separated from the hydrogen atom to which they were originally paired. These are: (1) molecularly adsorbed PH_3 dissociates into PH_2 and H across two dimer rows as shown in Fig. 6, (2) the PH_2 fragment of on-dimer PH_2+H undertakes transient excursions along the dimer rows (Fig. 7), and (3) the PH_2 fragment splits off PH_2+H across two dimer rows (Fig 10).

Additionally, we have shown that mobile PH_2 fragments become stabilized when recombining with a hemihydride. This hemihydride can either be the original hemihydride dimer from which the PH_2 fragment emanated, or a different hemihydride dimer that was encountered along the way. However, not all diffusing PH_2 fragments survive intact until such a pairing with hydrogen can occur. Some PH_2 fragments break up along the way and give rise to new set of observable STM features that are composed of one phosphorus atom and two hydrogen atoms. We will refer to this sequence of reactions and STM features in the following as the *PH_2 dissociation sequence.* It differs from the main (PH_3) dissociation sequence by involving one less hydrogen atom. These "missing" hydrogen atoms remain on the surface as hemihydride dimers that can be seen on Si(001) after PH_3 exposure.

Figure 12 shows an STM image sequence that illustrates the PH_2 dissociation sequence in action. The process starts with Fig. 12(a) in which an asymmetric PH_2+H feature can be seen on the right hand side while in the following image, Fig. 12(b), this feature has converted into a hemihydride feature (H). From the previous discussion we understand this as being due to PH_2 diffusion leaving behind a hemihydride species. In the same image [Fig. 12(b)] we also see a very bright protrusion appear towards the left hand side of the image, and one dimer row below the hemihydride. This protrusion is centered on the dimer row and it occurs at a site that was bare surface in the prior image [Fig. 12(a)]. The appearance of this protrusion just when a nearby PH_2+H converts into H strongly suggests that this feature is due to the migrating PH_2 fragment undergoing some form of dissociation event at this site. The process that has been captured in these images is the spontaneous dissociation of PH_2. This dissociation continues in Figs. 12(c) and (d), where the bright protrusion is seen to undergo two more transitions. The schematic valence structure diagrams in Figs. 12(e) to (h) outlines our structural interpretation of the processes occurring in this sequence. These assignments are supported by empty-state STM images [Figs. 12(i) to (k)] that were recorded in parallel.

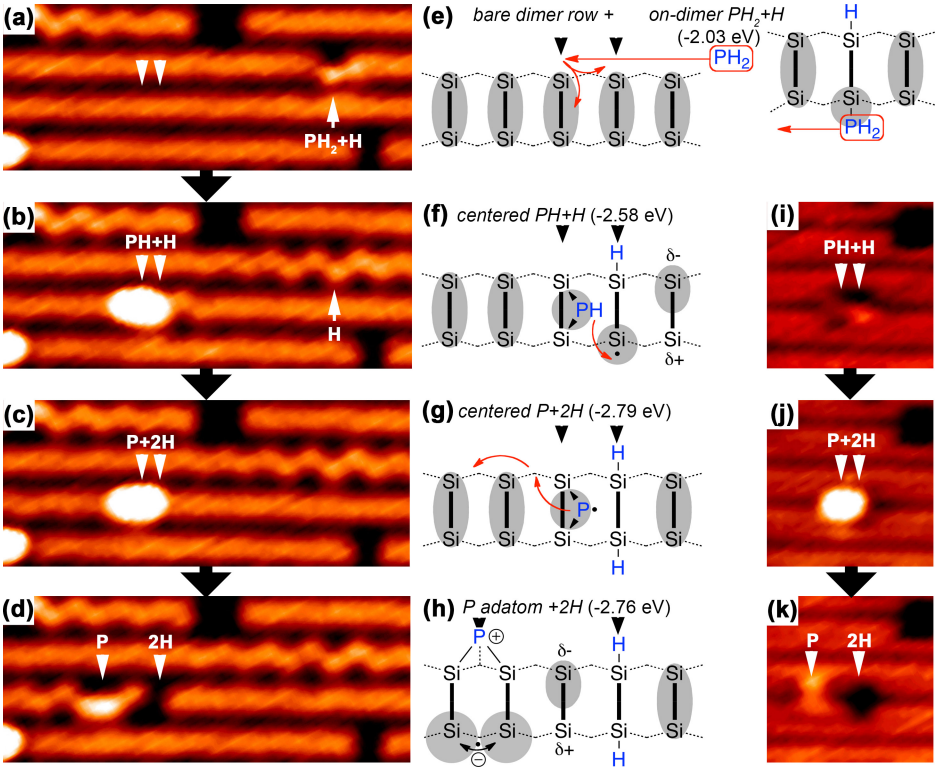

Figure 12: PH_2 dissociation sequence. (a-d) Sequence of STM images showing the same four dimer rows over a period of 22 minutes obtained using a filled-state sample bias of –2.0 V. (e-h) The corresponding schematic valence structure assignments in which gray shading is used to indicate those areas of the structure that are seen in the filled-state STM image. Given with each structure is the calculated adsorption energy using the 2D1R composite model. The PH_2+H feature in panel (a) transforms into hemihydride (H) in panel (b) while the PH_2 fragment diffuses onto and along a neighboring dimer row before dissociating to PH+H as illustrated in panel (f). The PH+H species further dissociates to form a P+2H in panel (c). In panel (d) the phosphorus atom diffuses to a more stable binding site, off-centre between two dimers and away from the monohydride dimer which images dark. Shown on the right-hand side (i-k) are three empty-state STM images at +1.2 V bias that were recorded simultaneously with the filled-state images (b-d). At this bias, the PH+H and P+2H features can be distinguished.

The initial PH_2 diffusion event is illustrated in Fig. 12(e) bringing the PH_2 fragment to a bare dimer site where it spontaneously dissociates into a PH+H species as shown in Fig. 12(f). In this species, the PH fragment is positioned centered above a Si-Si dimer to produce the very bright row centered protrusion seen in the filled-state image, Fig. 12(b). In this regard the PH+H feature seen here is similar to the more common PH+2H centered feature [see e.g. Fig. 5(b)]; however a subtle point of distinction in the filled-state image [Fig. 12(b)] is the notable offset shift of the row to the right of the main protrusion that occurs for the PH+H feature. In the corresponding empty-state image [Fig. 12(i)] we also observe a minor protrusion that is offset from the dimer row. These two attributes are neatly compatible with a hemihydride dimer that is adjacent to the dimer-centered PH fragment. In the subsequent filled-state image [Fig. 12(c)] the offset shift of the row next to the main centered protrusion has disappeared, and similarly in empty state [Fig. 12(j)] there is no longer a row-offset protrusion, but instead there is now a very bright row-centered protrusion in both filled and empty state. These images are

consistent with a feature that is symmetric about the dimer-row; the simplest interpretation is that a second hydrogen atom shifts from the phosphorus fragment so that we are left with a dimer-centered phosphorus atom and a monohydride dimer (2H). In this configuration, the phosphorus atom nominally carries the unpaired electron, which is consistent with the bright centered appearance in both filled and empty state images. The monohydride dimer is imaged as a depression in the empty state image, however in filled state this dimer is obscured by the very bright centered protrusion of the phosphorus atom. The final transition shown in Fig. 12(d,k) clearly reveals the dark monohydride in both biases. The phosphorus atom has shifted to the left, now bridging between two dimer ends as illustrated by the schematic in Fig. 12(h). We will discuss the precise imaging characteristics of this phosphorus adatom configuration further below. For the moment it suffices to say that it is not the phosphorus adatom itself that images in filled state, but the two bare silicon dimer ends on the opposite side [see gray shading in Fig. 12(h)]. Furthermore, the phosphorus adatom induces dimer pinning on both sides in filled state [Fig. 12(d)]. This pinning extends away over several dimers on the left hand side of the defect. On the right hand side, only the single bare dimer between the phosphorus adatom and the monohydride dimer is pinned.

Included in Fig. 12 for each of the observed species is the calculated energy using the 2D1R composite model. These energies confirm that the sequence of observed species PH_2+H [Fig. 12(e)], PH+H [Fig. 12(f)], and P+2H [Fig. 12(g)] results in progressively lower energies of -2.03, -2.58, and -2.79 eV, respectively. Hence, this reaction sequence, much like the PH_3 main sequence, is driven by a gain in thermodynamic stability as hydrogen atoms are sequentially transferred from the phosphorus atom to nearby dimers on the silicon surface. We note that these energies for the latter two species – PH+H and P+2H - account for the hemihydride that was left behind when the PH_2 fragment departed from the PH_2+H species. This is achieved in our 2D1R composite model by describing the hemihydride and the PH+H or P+2H species on separate clusters, and adjusting the relative energy expression (Eq. 2) above as follows

$$\Delta E = E_{cluster+PH+H} + E_{cluster+H} - 2\,E_{cluster} - E_{PH3(gas)}. \qquad (5)$$

to account for the "spread" of the phosphine adsorbate over separate two clusters. This equation is written out here for the example of the PH+H adsorbate, but equivalently applies to other cases where fragments of a PH_3 adsorbate become spatially separated from one another.

A similar approach was used to calculate the energy of the final structure [Fig. 12(d)] in the Fig. 12 image sequence. Here, we regard the end-bridge phosphorus adatom, the monohydride dimer, and the "left-behind" hemihydride as all effectively separated from another, and thus, we attach these fragments to three separate clusters in order to evaluate a net

adsorption energy. The computed value of -2.76 eV of this fully separated configuration is only very slightly larger than the value of -2.79 eV obtained for the P+2H species [Fig. 12(c)], from which the separated configuration is seen to arise. Entropic effects, which are not explicitly included in our energy expressions, are likely to favor the separated configuration and render the separation reaction exergonic.

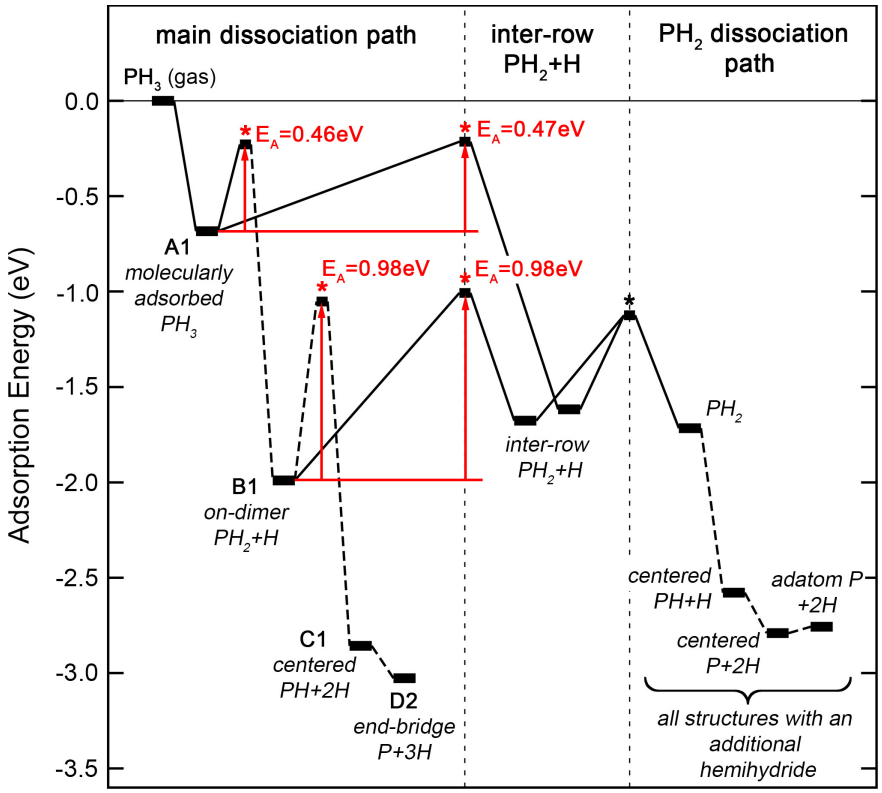

FIG. 13: Overview potential energy profile contrasting the energetics of the main PH_3 dissociation sequence on the left with that of the PH_2 dissociation sequence on the right. Selected activation energies that are relevant to the balance between these two sequences are highlighted using red-colored arrows. Metastable structures and transition states are indicated using long and short horizontal bars, respectively. Transition states are further labeled using stars (*) and linked to their immediate initial and final configurations using solid lines. Abbreviated, multi-step transitions are indicated using dashed lines. This figure combines energies that were calculated using the 2D1R, 3D1R, and 3D2R cluster composite models. Note that the abbreviated, dashed-line transitions may involve other activation energies that are rate determining for the transition itself, but that are not relevant to the balance between the two dissociation sequences.

With Figure 13 we now provide a composite overview of the energetics of the PH_3 main dissociation sequence, the PH_2 dissociation sequence, and the key activation energies that link between these two sequences. On the left-hand side we have the main dissociation sequence in abbreviated form, highlighting only the major species involved, namely molecularly adsorbed PH_3 (structure **A1**), on-dimer PH_2+H (**B1**), centered PH+2H (**C1**) and fully dissociated P+3H (**D2**). On the right-hand side the intermediates of the PH_2 dissociation sequence are shown, namely, the highly mobile PH_2 species, PH+H, P+2H, and then the phosphorus adatom separated from the monohydride (2H). Bridging between these two dissociation

sequences we have in the center the two inter-row PH_2+H structures that arise from structures **A1** (PH_3) and **B1** (on-dimer PH_2+H) via an inter-row hydrogen shift [*cf.* Fig. 6] and an inter-row PH_2 shift [*cf.* Fig. 11], respectively. Their energies of -1.68 and -1.62 eV are very slightly different due to the relative position of PH_2 and H fragments on the two adjacent rows, but close to the energy of -1.72 eV of PH_2 when completely separated from H. The latter structure is the entry point for the PH_2 dissociation sequence, and it is accessed from the inter-row PH_2+H structures via inter-dimer PH_2 diffusions steps along the row, which have an activation energy of 0.58 eV. This again assumes diffusion via the positive charge state of PH_2 as discussed above.

The main point to take from Fig. 13 is the close competition between key barriers of the PH_3 main dissociation sequence, and those that facilitate the spatial separation of PH_2 and H fragments. These barriers are highlighted using red colored arrows in Fig. 13. The molecular adsorbate (structure **A1**) experiences a barrier of 0.46 eV to shift a hydrogen atom to an adjacent dimer on the same row; a path that leads to the observable on-dimer PH_2+H species (**B1**) of the main dissociation sequence. Competing with this barrier is the inter-row H shift with an activation energy of 0.47 eV which produces inter-row PH_2+H, and subsequently diffusing PH_2 which may either stabilize along the PH_2 dissociation path or by recombining with H to form on-dimer PH_2+H. The near equality of these two barriers suggests that both types of H-shift reactions should occur, which explains in part the diversity of phosphine species observed in our image data. Similarly, the on-dimer PH_2+H species **B1** experiences an effective barrier of 0.98 eV to dissociate into the PH+2H species **C1** along the main sequence. Here too, an inter-row reaction, namely, the inter-row PH_2 shift is in competition with an activation energy that also computes to 0.98 eV. The PH_2 fragment of on-dimer PH_2+H may also undertake short-lived excursions away from H atom along the dimer row, which presents a barrier of 0.93 eV [cf. Fig. 9]. Either reaction creates mobile PH_2 fragments that are separated from H. These fragments in turn can either recombine with H to PH_2+H and progress along the main sequence, or dissociate along the PH_2 dissociation sequence. Again, the near equality of the relevant barriers suggests that these processes all occur. This is consistent with the numerous types of transitions seen in our experiments.

F. Isolated Phosphorus Adatoms

We now consider in closer detail the phosphorus adatom species [Fig. 12(h)] that we have attributed to the images in Figs. 12(d) and (k). Close-up images with better resolution of the same type of STM feature are shown in Fig. 14(a) and (b). In the empty-state image [Fig. 14(b)] this species has a distinct T-shaped protrusion, so we label it the *T-shaped feature*. As we have already stated, this image feature corresponds to an isolated phosphorus adatom that is bonded to two adjacent dimer

ends. The gray shading in the schematics Fig. 14(c,d) is drawn as a guide to the eye for interpreting the contrast seen in the STM images. Together the P atom and the two dangling bonds give rise to the characteristic T-shaped appearance in the empty state image.

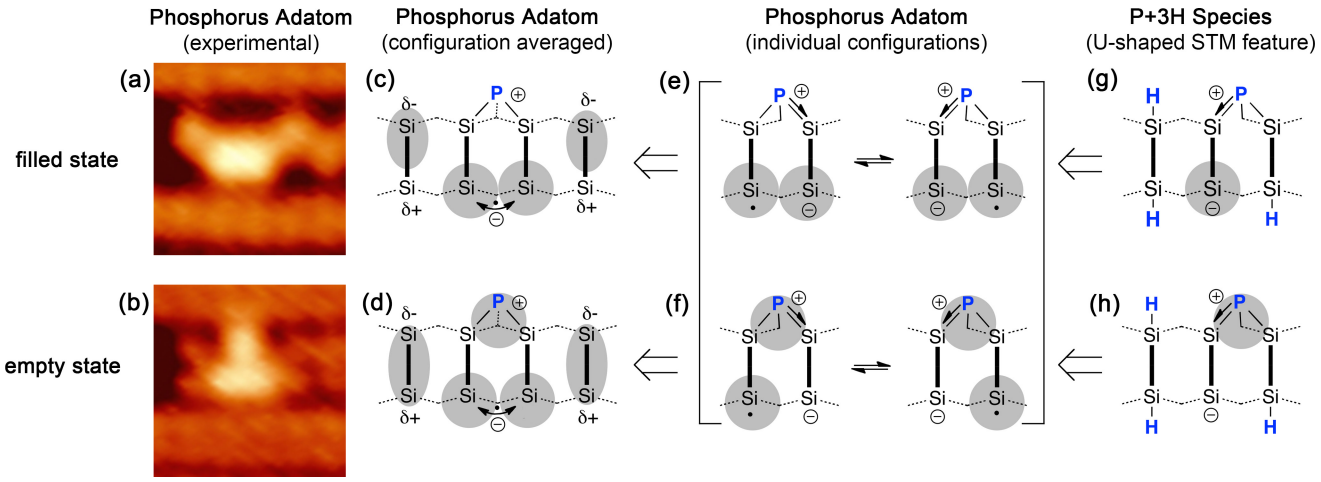

FIG. 14: (a,b) High-resolution, filled and empty state images of the *T-shaped* STM feature corresponding to an isolated phosphorus adatom on the Si(001) surface. (c-h) The expected appearance of an isolated P adatom in STM images can be rationalized by analogy to the known U-shaped feature, a P adatom surrounded by three hydrogen atoms [*cf.* Fig. 5(c,f)]. Schematic valence structure diagrams outline this analogy, with imaging sites in filled and empty state indicated by grey shading. STM images in (a) and (b) were recorded using a sample bias of -1.6 and +1.2 V, respectively, and a set point current of 0.2 nA.

The reasons for why these sites image as they do can be understood by analogy to the closely related P+3H structure **D2**, in which the P adatom is surrounded by three hydrogen atoms. Described in detail in Refs. 16 and 17, the bonding of the phosphorus adatom in the P+3H structure is somewhat unusual in that a backbond between one of the dimers and a subsurface silicon atom is broken (see e.g. Fig. 8 in Ref. 17). This results in a nominal positive valence charge at the phosphorus adatom and a double occupancy and nominal negative charge at the bare silicon dimer end. Accordingly, these two sites image in empty and filled state STM images as illustrated by gray shading in Fig. 14(h) and (g), respectively. When fully geometry optimized, an isolated P adatom also adopts an asymmetric geometry similar to that of the P+3H feature, with again one of the backbonds broken. Hence, by analogy to the P+3H feature, we can plausibly expect the isolated P adatom to image bright in empty state at the P atom and bright in filled state at the doubly occupied dangling bond, as shown in Fig. 14(e) and (f). The dangling bond of the adjacent dimer end is singly occupied (indicated by a dot in Fig. 14(e) and (f)] and is thus expected to appear bright in both filled and empty state. Taken together, we have both of the bare Si dimer ends opposite to the P adatom imaging bright in filled state, whereas the phosphorus adatom and only one of the two dimer ends are bright in empty state. This is the imaging pattern expected for a phosphorus adatom if it were locked into a *single* asymmetric

configuration. However, under the conditions of our experiment, the asymmetric end-bridge configuration is in rapid thermal equilibrium with its mirror image configuration as illustrated in Fig. 14(e,f). The calculated activation energy between these two mirror-image configurations is only 0.11 eV. Combined with a calculated attempt frequency of 6×10^{12} s^{-1}, we obtain an estimated switching rate of order 10^{11} s^{-1} at room temperature. This is very much faster than the experimental imaging rate (minutes) and hence a symmetric average is observed in experiment [Fig. 14(a,b)] in which both of the bare Si dimer ends image bright in filled and empty state. On the other side of the feature, the P adatom images brightly in empty state only, which produces the characteristic T-shape appearance at this bias.

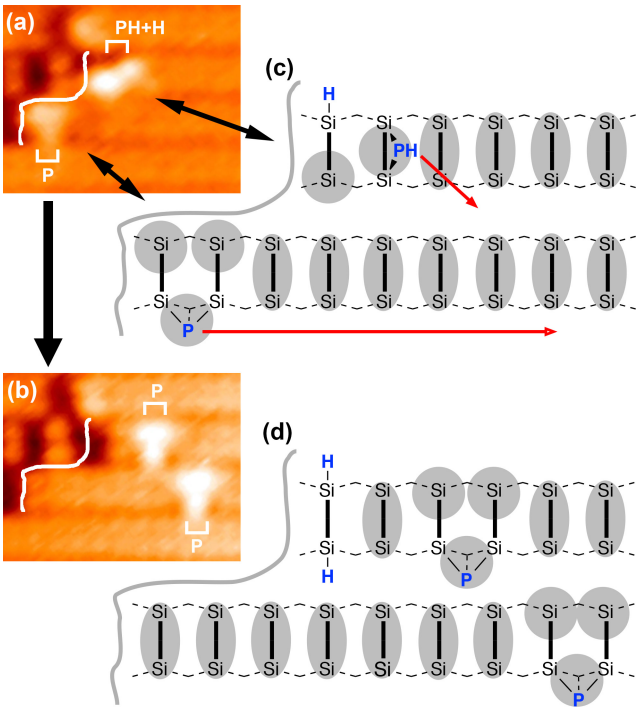

FIG. 15: (a,b) High-resolution empty state STM images of the Si(001) surface showing the diffusion of two phosphorus adatoms in the vicinity of a large surface defect complex (upper left corner). A white curvy line is used to indicate the boundary of the defect complex. Phosphorus adatoms are apparent as bright T-shaped protrusions. The two images taken in succession show two phosphorus adatoms diffusing over several dimers to the right. Schematic illustrations of the corresponding chemical structures are shown in panels (c,d).

Phosphorus adatoms on the Si(001) surface are also observed to be somewhat mobile, being able to shift along the dimer row. This mobility is illustrated by the sequence of two empty-state STM images shown in Figs. 15(a) and (b). In the upper left corner of these images there is a larger defect complex (a cluster of several dimer vacancies) however towards the lower left corner of Fig. 15(a), the T-shaped feature of a phosphorus adatom can be seen. In the second image, Fig 15(b), the feature has shifted seven dimers to the right, and is now seen in the lower right-hand corner of the image. In the row above, and slightly to the left, a second phosphorus adatom can be seen as a T-shaped feature. This second phosphorus adatom most

likely arises from the bright centered feature in Fig. 15(a), which we attribute to a PH+H species (i.e. the same species seen in Fig. 12(b,f,i) above). The filled-state STM images of this transition (not shown here) are consistent with this interpretation. Schematic chemical structures shown Figs. 15(c) and (d) illustrate the species involved in this transition. We believe this is the first direct observation of single phosphorus adatom diffusing on the silicon (001) surface. Brocks et al. [77] and Bennett et al. [28] have reported DFT-calculated activation energies for P adatom diffusion of 0.8 and 0.94 eV, respectively. This corresponds to an estimated average timescale of transition (or inverse rate) of between 0.3 s and 10 min, respectively, at room temperature using a typical attempt frequency of 10^{13} s^{-1}. This range of timescales is consistent with the observation of such diffusion events in our STM experiments.

IV. SUMMARY AND CONCLUSIONS

In summary, detailed quantum-chemical cluster calculations have been applied to develop a comprehensive understanding of the dissociation of phosphine on the Si(001) surface. Transition-state calculations provide a chemical "interpolation" between the experimentally observed intermediates leading to a complete step-by-step mechanism of the PH_3 main dissociation sequence that gives to PH_2+H, PH+2H, and P+3H as observable species. Our calculated reaction barriers are consistent with the observed reaction rates. These calculated barriers and associated rates explain why certain intermediates are observed in our STM experiments, and others are not. In addition, new STM image data is reported which allows our calculations to delineate between the main dissociation sequence and a secondary sequence that commences with a diffusing PH_2 fragment. This secondary sequence produces PH+H, P+2H, and phosphorus adatoms (P) as observable species. We explain how the facile diffusion of PH_2 fragments from dimer to dimer at room temperature (Figs. 7 and 10), in conjunction with two types of inter-row reactions (Figs. 6 and 11), provides the mechanistic link between these two dissociation sequences. We further show how the activation energies of these diffusion and inter row reactions are in close competition with the activation energies of main sequence dissociation. This competition explains why the products of both sequences are observed after phosphine dosing, including the abundance of hemihydride dimers.

ACKNOWLEDGMENTS

O.W., D.R.M, and M.Y.S. acknowledge the support of the Australian Research Council (ARC) Centre of Excellence for Quantum Computation and Communication Technology (project number CE110001027). M.Y.S. is also supported by the U.S. National Security Agency and the U.S. Army Research Office under contract number W911NF-08-1-0527. M.Y.S. and

N.A.M. acknowledge the ARC for providing fellowships. Computing support was provided by the Australian National Computational Infrastructure (NCI).

REFERENCES

1. S. M. Sze and K. K. Ng, "Physics of Semiconductor Devices", Wiley (2007).
2. M. L. Yu and B. S. Meyerson, J. Vac. Sci. Technol. A 2 (1984) 446.
3. M. L. Yu, D. J. Vitkavage, and B. S. Meyerson, J. Appl. Phys. 59 (1986) 4032.
4. Y. Wang, M. J. Bronikowski, and R. J. Hamers, J. Phys. Chem., 98 (1994) 5966.
5. Y. Wang, X. Chen, and R. J. Hamers, Phys. Rev. B 50 (1994) 4534.
6. M. L. Colaianni, P. J. Chen, and J. T. Yates, Jr., J. Vac. Sci. Technol. A 12 (1994) 2995.
7. L. Kipp, R. D. Bringans, D. K. Biegelsen, J. E. Northrup, A. Garcia, and L.-E. Swartz, Phys. Rev. B 52 (1995) 5843.
8. N. Maity, L.-Q. Xia, S. E. Roadman, and J. R. Engstrom, Surf. Sci. 344 (1995) 203.
9. J. Shan, Y. Wang, and R. J. Hamers, J. Phys. Chem. 100 (1996) 4961.
10. D.-S. Lin, T.-S. Ku, and T.-J. Sheu, Surf. Sci. 424 (1999) 7.
11. F. Hirose and H. Sakamoto, Surf. Sci. 430 (1999) L540.
12. Y. Tsukidate and M. Suemitsu, Appl. Surf. Sci. 151 (1999) 148.
13. D.-S. Lin, T.-S. Ku, and R.-P. Chen, Phys. Rev. B 61 (2000) 2799.
14. H.-W. Tsai and D.-S. Lin, Surf. Sci. 482–485 (2001) 654.
15. N. J. Curson, S. R. Schofield, M. Y. Simmons, L. Oberbeck, J. L. O'Brien, and R. G. Clark, Phys. Rev. B 69 (2004) 195303.
16. H. F. Wilson, O. Warschkow, N. A. Marks, S. R. Schofield, N. J. Curson, P. V. Smith, M. W. Radny, D. R. McKenzie, and M. Y. Simmons, Phys. Rev. Lett. 93 (2004) 226102.
17. O. Warschkow, H. F. Wilson, N. A. Marks, S. R. Schofield, N. J. Curson, P. V. Smith, M. W. Radny, D. R. McKenzie, and M. Y. Simmons, Phys. Rev. B. 72 (2005) 125328.

18. S. R. Schofield, N. J. Curson, O. Warschkow, N. A. Marks, H. F. Wilson, M. Y. Simmons, P. V. Smith, M. W. Radny, D. R. McKenzie, and R. G. Clark, J. Phys. Chem. B 110 (2006) 3173.

19. S. R. McKibbin, W. R. Clarke, A. Fuhrer, T. C. G. Reusch, M. Y. Simmons, Appl. Phys. Lett. 95, 233111 (2009).

20. S. R. McKibbin, C. M. Polley, G. Scappucci, J. G. Keizer, and M. Y. Simmons, Appl. Phys. Lett. 104, 123502 (2014).

21. P.-L. Cao, L.-Q. Lee, J.-J. Dai, and R.-H. Zhou, J. Phys.: Condens. Matter 6 (1994) 6103.

22. R. Miotto, G. P. Srivastava, and A. C. Ferraz, Phys. Rev. B 63 (2001) 125321.

23. R. Miotto, G. P. Srivastava, R. H. Miwa, and A. C. Ferraz, J. Chem. Phys. 114, (2001) 9549.

24. R. Miotto, G. P. Srivastava, and A. C. Ferraz, Surf. Sci. 482–485 (2001) 160.

25. R. Miotto, A. C. Ferraz, and G.P. Srivastava, Braz. J. Phys. 32 (2002) 392.

26. T. L. McDonell, N. A. Marks, O. Warschkow, H. F. Wilson, P. V. Smith, and M. W. Radny, Phys. Rev. B 72, 193307 (2005).

27. H. F. Wilson, O. Warschkow, N. A. Marks, N. J. Curson, S. R. Schofield, P. V. Smith, T. C. G. Reusch, M. W. Radny, D. R. McKenzie, and M. Y. Simmons, Phys. Rev. B 74 (2006) 195310.

28. J. M. Bennett, O. Warschkow, N. A. Marks, and D. R. McKenzie, Phys. Rev. B 79 (2009) 165311.

29. J. M. Bennett, O. Warschkow, N. A. Marks, and D. R. McKenzie, Phys. Rev. B 82 (2010) 235417.

30. B. E. Kane, Nature, 393 (1998) 133.

31. A. M. Stoneham, A. J. Fisher, and P. T. Greenland, J. Phys. Condens. Matter 15 (2003) L447–L451.

32. F. J. Ruess, L. Oberbeck, M. Y. Simmons, K. E. J. Goh, A. R. Hamilton, T. Hallam, S. R. Schofield, N. J. Curson, and R. G. Clark, Nano Letters 4 (2004) 1969.

33. T. C. Shen, J. S. Kline, T. Schenkel, S. J. Robinson, J. Y. Ji, C. Yang, R. R. Du, and J. R. Tucker, J. Vac. Sci. Tech. B 22 (2004) 3182.

34. L. C. L. Hollenberg, A. D. Greentree, A. G. Fowler, and C. J. Wellard, Phys. Rev. B 74 (2006) 045311.

35. L. C. L. Hollenberg, A. S. Dzurak, C. Wellard, A. R. Hamilton, D. J. Reilly, G. J. Milburn, and R. G. Clark, Phys. Rev. B 69 (2004) 113301.

36. M. Y. Simmons, F. J. Rueß, K. E. J. Goh, T. Hallam, S. R. Schofield, L. Oberbeck, N. J. Curson, A. R. Hamilton, M. J. Butcher, R. G. Clark and T. C. G Reusch, Molecular Simulation, 31 505 (2005).

37. F.J. Ruess, W. Pok, T. C. G. Reusch, M. J. Butcher, K. E. J. Goh, L. Oberbeck, G. Scappucci, A. R. Hamilton, and M. Y. Simmons, Small 3 (2007) 563.

38. J. J. L. Morton, D. R. McCamey, M. A. Eriksson and S. A. Lyon, Nature 479, 345 (2011).

39. B. Weber, S. Mahapatra, H. Ryu, S. Lee, A. Fuhrer, T. C. G. Reusch, D. L. Thompson, W. C. T. Lee, G. Klimeck, L. C. L. Hollenberg, M. Y. Simmons, Science 335, 64 (2012).

40. M. Fuechsle, J. A. Miwa, S. Mahapatra, H. Ryu, S. Lee, O. Warschkow, L. C. L. Hollenberg, G. Klimeck, and M. Y. Simmons, Nature Nanotechnol. 7, 242 (2012).

41. M. Fuechsle and M.Y. Simmons, Single-Atom Nanoelectronics (pp. 61-89, ed. E. Prati and T. Shinada, Pan Stanford Publishing, Singapore, 2013).

42. J. L. O'Brien, S. R. Schofield, M. Y. Simmons, R. G. Clark, A. S. Dzurak, N. J. Curson, B. E. Kane, N. S. McAlpine, M. E. Hawley, and G. W. Brown, Phys. Rev. B 64 (2001) 161401.

43. S. R. Schofield, N. J. Curson, M. Y. Simmons, F. J. Ruess, T. Hallam, L. Oberbeck, and R. G. Clark, Phys. Rev. Lett. 91 (2003) 136104.

44. J. W. Lyding, G. C. Abeln, T. -C. Shen, C. Wang, and J. R. Tucker, J. Vac. Sci. Technol. B 12, 3735 (1994).

45. J. W. Lyding, T.-C. Shen, J. S. Hubacek, J. R. Tucker, and G. C. Abeln, Appl. Phys. Lett. 64 (1994) 2010.

46. T.-C. Shen, C. Wang, G. C. Abeln, J. R. Tucker, J. W. Lyding, Ph. Avouris, and R. E. Walkup, Science 268 (1995) 1590.

47. J. R. Tucker and T. C. Shen, Int. J. Circuit Theory Appl. 28 (2000) 553.

48. M. J. Frisch, G. W. Trucks, H. B. Schlegel, G. E. Scuseria, M. A. Robb, J. R. Cheeseman, G. Scalmani, V. Barone, B. Mennucci, G. A. Petersson, H. Nakatsuji, M. Caricato, X. Li, H. P. Hratchian, A. F. Izmaylov, J. Bloino, G. Zheng, J. L. Sonnenberg, M. Hada, M. Ehara, K. Toyota, R. Fukuda, J. Hasegawa, M. Ishida, T. Nakajima, Y. Honda, O. Kitao, H. Nakai, T. Vreven, J. A. Montgomery, Jr., J. E. Peralta, F. Ogliaro, M. Bearpark, J. J. Heyd, E. Brothers, K. N. Kudin, V. N. Staroverov, T. Keith, R. Kobayashi, J. Normand, K. Raghavachari, A. Rendell, J. C. Burant, S. S. Iyengar, J. Tomasi, M. Cossi, N. Rega, J. M. Millam, M. Klene, J. E. Knox, J. B. Cross, V. Bakken, C. Adamo, J. Jaramillo, R. Gomperts, R.

E. Stratmann, O. Yazyev, A. J. Austin, R. Cammi, C. Pomelli, J. W. Ochterski, R. L. Martin, K. Morokuma, V. G. Zakrzewski, G. A. Voth, P. Salvador, J. J. Dannenberg, S. Dapprich, A. D. Daniels, O. Farkas, J. B. Foresman, J. V. Ortiz, J. Cioslowski, and D. J. Fox, Gaussian 09, Revision D.01, Gaussian, Inc., Wallingford CT, 2013.

49. O. Warschkow, T. L. McDonell, and N. A. Marks, Surface Science 601 (2007) 3020-3033.

50. O. Warschkow, I. Gao, S. R. Schofield, D. R. Belcher, M. W. Radny, S. A. Saraireh and P. V. Smith, Phys. Chem. Chem. Phys. 11 (2009) 2747.

51. O. Warschkow, S. R. Schofield, N. A. Marks, M. W. Radny, P. V. Smith, and D. R. McKenzie, Phys. Rev. B 77 (2008) 201305.

52. D. R. Belcher, S. R. Schofield, O. Warschkow, M. W. Radny, P. V. Smith, J. Chem. Phys. 131 (2009) 104707.

53. O. Warschkow, N. A. Marks, S. R. Schofield, M. W. Radny, P. V. Smith, D. R. McKenzie, Surf. Sci. 604, 235 (2010).

54. O. Warschkow, D. R. Belcher, S. R. Schofield, P. V. Smith, and M. W. Radny, Phys. Rev. B 84 (2011) 153302.

55. G. Scappucci, O. Warschkow, G. Capellini, W. M. Klesse, D. R. McKenzie, and M.Y. Simmons, Phys. Rev. Lett. 109 (2012) 076101.

56. S. R. Schofield, O. Warschkow, D. R. Belcher, K. A. Rahnejat, M. W. Radny, and P. V. Smith, J. Phys. Chem. C 117 (2013) 5736.

57. A. D. Becke, Phys. Rev. A 38, 3098 (1988).

58. C. Lee, W. Yang, and R. G. Parr, Phys. Rev. B 37, 785 (1988).

59. J. P. Perdew, J. A. Chevary, S. H. Vosko, K. A. Jackson, M. R. Pederson, D. J. Singh, and C. Fiolhais, Phys. Rev. B, 46, 6671 (1992).

60. J. P. Perdew, K. Burke, and Y. Wang, Phys. Rev. B 54, 16533 (1996).

61. The purpose of the monohydride termination in our slab-model template is to ensure that surface Si-Si dimers in the template are flat, and not buckled as would be the case for the bare Si(001) surface. This is important because otherwise our procedure to determine the constrained positions of the cluster-terminating hydrogen atoms would “imprint” a specific dimer-buckling orientation into the cluster termination. A flat-dimer template ensures that our cluster-

termination is symmetric with respect to dimer buckling. We stress that the monohydride hydrogen atoms of the template do not become a part of the cluster termination.

62. D. F. Tracey, B. Delley, D. R. McKenzie, and O. Warschkow, AIP Advances 3, 042117 (2013).

63. P. A. Redhead, Vacuum 12, 203 (1962).

64. C. Peng and H.B. Schlegel, Israel J. Chem. 33, 449 (1993).

65. G. H. Vineyard, J. Phys. Chem. Solids 3, 121 (1957).

66. H.S. Johnston and J. Heincklen, J. Phys. Chem. 66, 532 (1962).

67. Brown, R.L., J. Res. Nat. Bur. Stand. 86, 357 (1981).

68. J.L. Pitters, P.G. Piva, and R.A. Wolkow, J. Vac. Sci. Tech. B 30, 021806 (2012).

69. M. W. Radny, P. V. Smith, T. C. G. Reusch, O. Warschkow, N. A. Marks, H. F. Wilson, S. R. Schofield, N. J. Curson, D. R. McKenzie, and M. Y. Simmons, Phys. Rev. B 76 155302 (2007).

70. T. C. G. Reusch, O. Warschkow, M. W. Radny, P. V. Smith, N. A. Marks, N. J. Curson, D. R. McKenzie, M. Y. Simmons, Surf. Sci. 601, 4036 (2007).

71. B. Naydenov, M. Mantega, I. Rungger, S. Sanvito, and J. J. Boland, Phys. Rev. B 84, 195321 (2011).

72. M. Mantega, I. Rungger, B. Naydenov, J. J. Boland, and S. Sanvito, Phys. Rev. B 86, 035318 (2012).

73. M. W. Radny, P. V. Smith, T. C. G. Reusch, O. Warschkow, N.A. Marks, H.F. Wilson, N. J. Curson, S. R. Schofield, D. R. McKenzie, and M. Y. Simmons, Phys. Rev. B 74, 113311 (2006).

74. M. W. Radny, P. V. Smith, T. C. G. Reusch, O. Warschkow, N. A. Marks, H. Q. Shi, D. R. McKenzie, S. R. Schofield, N. J. Curson, and M. Y. Simmons, J. Chem. Phys. 127, 184706 (2007).

75. T. C. G. Reusch, M. W. Radny, P. V. Smith, O. Warschkow, N. A. Marks, N.J. Curson, D. R. McKenzie, M. Y. Simmons, J. Phys. Chem. C 111, 6428 (2007).

76. This is necessary, because the conduction band in a cluster model tends to be insufficiently dispersed to act as an acceptor for the unpaired electron. However, for our purpose of calculating diffusion barriers, this approximation is adequate because the charge of the cluster directly determines the occupancy of the Si-Si-PH_2 dangling bond orbital. We

note that this is different in periodic slab models of dangling bond defects where even in a neutral cell calculation the dangling bond electron may spontaneously ionize into a dispersed conduction band.

77. G. Brocks, P. J. Kelly, and R. Car, Surf. Sci. 269–270, 860 (1992).